

1 **Hillslopes in Headwaters of Qinghai-Tibetan Plateau as Hotspots for**
2 **Subsurface Dissolved Organic Carbon Processing during Permafrost Thaw**

3
4 **Yuqin Sun^{1,2,3}, Kale Clauson⁴, Min Zhou¹, Ziyong Sun⁵, Chunmiao Zheng^{2,3} and Yan**
5 **Zheng^{2,3*}**

6
7 ¹ College of Engineering, Peking University, Beijing, 100871, China.

8 ² State Environmental Protection Key Laboratory of Integrated Surface Water-Groundwater
9 Pollution Control, School of Environmental Science and Engineering, Southern University of
10 Science and Technology, Shenzhen, 518055, China.

11 ³ Guangdong Provincial Key Laboratory of Soil and Groundwater Pollution Control, School of
12 Environmental Science and Engineering, Southern University of Science and Technology,
13 Shenzhen, 518055, China.

14 ⁴ School of Earth and Environmental Sciences, Queens College, City University of New York,
15 Flushing, NY 11367, USA.

16 ⁵ School of Environmental Studies, China University of Geosciences, Wuhan, 430074, China.

17
18 Corresponding author: Yan Zheng (yan.zheng@sustech.edu.cn) ORCID 0000-0001-5256-9395

19
20
21
22 **Key Points**

- 23 • Surface and subsurface waters in an alpine watershed of Qinghai-Tibetan Plateau contain
24 permafrost sourced bioavailable DOC.
- 25 • Hillslopes in headwaters of QTP are hotspots for subsurface DOC processing before it
26 reaches the main river during seasonal thaw.
- 27 • New constraint is placed on hillslope groundwater mean transit time (~6 to 20 days) from
28 the DOC loss and the biodegradation kinetics.
29

30 **Abstract**

31 Climate warming has accelerated thawing of northern permafrost, resulting in changes to the
32 supply of dissolved organic carbon (DOC) to inland waters with uncertain fate. Extensive surface
33 – groundwater interactions occur in alpine permafrost watersheds and likely influence DOC
34 processing differently than systems with limited interactions. Here, we quantify and characterize
35 DOC in waters collected from eight water types sampled across a small (25 km²) alpine (elevation
36 2960 to 4820 m a.s.l) watershed in the Qinghai-Tibetan Plateau (QTP) containing variably
37 degraded permafrost. Three types of water (thermokarst ponds, red mud gully and seepage-I)
38 contained high DOC concentrations (5.2 to 22.6 mg/L, n=38), with C contributions
39 predominantly from frozen soil meltwater. Spatial patterns of DOC in stream (0.3 to 4.8 mg L⁻¹,
40 n=41), and subsurface waters (0.4 to 3.8 mg/L, n=34), all contained frozen soil meltwater C as
41 constrained by $\delta^{18}\text{O}$ and electrical conductivity, reflecting surface – groundwater exchanges in
42 the upper-, mid- and lower stretches of the watershed. Further, patterns of increasing DOC loss
43 (ΔDOC) in subsurface waters with decreased proportions of protein-like organic matter and
44 SUVA_{254} , suggest subsurface microbial processing. Using previously established biodegradation
45 DOC kinetics (0.06 d⁻¹) from the QTP, the groundwater transit time is estimated to be between 6
46 and 20 days based on ΔDOC changes of 32% and 74% for July and September, respectively.
47 Mass balance of DOC inputs and export fluxes demonstrate nearly half of all DOC was lost in
48 this small watershed, indicating hillslopes are hotspots for DOC processing, with subsurface
49 environments playing a key role.

50

51 **Plain Language Summary**

52 Climate warming leads to thawing of the northern permafrost that has increased the release of
53 organic carbon, previously regarded as “stable”, into streams and rivers. Recent laboratory
54 studies of Arctic permafrost show the rapid biodegradation of permafrost-derived organic carbon,
55 but is it true? For this, we turn to a small, alpine watershed in the Qinghai-Tibetan Plateau with
56 a gradient of permafrost degradation. First, we provide rare field evidence for widespread
57 permafrost sourced organic carbon in a variety of water types based upon its optical properties.
58 Secondly, we use stable isotopes and electrical conductivity as “conservative” tracers to compare
59 with dissolved organic carbon that are “reactive” to estimate the loss of organic carbon from its

60 upgradient source to the downslope sampling location. The extent of the loss of DOC in
61 subsurface environment is dependent on the travel time of the groundwater along the hillslope.
62 The DOC originating from permafrost soil is quickly dispersed in the watershed, shedding light
63 on previously poorly constrained surface water – groundwater interaction in such settings.
64 Finally, a mass budget finds a large loss of organic carbon within the watershed. Therefore,
65 hillslopes act as hotspots for permafrost-derived organic carbon processing.

66

67 **Keywords**

68 Qinghai-Tibetan Plateau, Dissolved organic carbon, Permafrost, Alpine watershed,
69 Groundwater transit time, Fluorescence spectroscopy

70

71 **1 Introduction**

72 Northern permafrost, including 42% of the areal extent of Qinghai-Tibetan Plateau
73 (QTP), is estimated to account for >20% of total global soil organic carbon (SOC) pool of 1832
74 $\times 10^{12}$ kg [Tarnocai *et al.*, 2009; Wang *et al.*, 2020]. Models assessing biogeochemical cycles of
75 soil C have raised the concern that thaw and degradation may reverse northern permafrost regions
76 from a current C sink to a net source, under future warming trajectories [McGuire *et al.*, 2018;
77 Turetsky *et al.*, 2020; Wang *et al.*, 2020]. Thawed permafrost SOC enters pore waters as dissolved
78 organic carbon (DOC), a proportion of which is exported to aquatic systems to become
79 components of in-stream carbon cycling. About 15% of permafrost SOC may enter aquatic
80 systems over the next 300 years under future warming scenarios [McGuire *et al.*, 2018]. In the
81 high latitude Arctic permafrost region, CO₂ evasion from inland waters is estimated to account
82 for between 40×10^9 to 84×10^9 kg C yr⁻¹ [McGuire *et al.*, 2009], but little is known about CO₂
83 evasion from inland waters in high altitude permafrost regions such as the QTP.

84 Streams and rivers are known hotspots for DOC processing [Raymond *et al.*, 2013]. This
85 notion is further reinforced in a compilation of DOC losses during passages from terrestrial
86 sources to sea, highlighting microbially mediated respiration of DOC in response to retention
87 time scales [Catalan *et al.*, 2016]. Globally, streams and rivers are responsible for 1.8×10^{12} kg
88 C yr⁻¹ out of the total of 2.1×10^{12} kg C yr⁻¹ CO₂ evasion from inland waters [Raymond *et al.*,
89 2013]. The total evasion has been revised upward to 3.9×10^{12} kg C yr⁻¹ [Drake *et al.*, 2018],

90 owing to more observational data. However, this flux is likely an underestimation. Due to lack
91 of hydrologic data in small-sized headwater streams, it has been suggested that C evasion from
92 small streams may be substantial but remain unaccounted for [*Drake et al.*, 2018; *Raymond et*
93 *al.*, 2013]. Here, we describe ambiguities in DOC processing associated with permafrost thawing
94 and degradation first in lateral flow dominated Arctic watersheds, then in alpine watersheds with
95 extensive surface water – groundwater interactions along the hillslopes.

96 The apparently wide variability in DOC processing observed in the Arctic permafrost
97 regions can be reconciled by considering the evolving nature of the SOC sources and time it takes
98 for the SOC leachate to infiltrate and move laterally into the stream (SOC to porewater DOC,
99 then subsequently DOC in streams). All of these processes are likely to alter under ongoing
100 climate change. Arctic river waters sampled at large basin scales (8000 to 855,000 km²) have
101 been shown to contain highly aromatic and less biologically labile DOC with young (390-1440
102 yr BP) radiocarbon age [*Balcarczyk et al.*, 2009; *Guo and Macdonald*, 2006; *Guo et al.*, 2007;
103 *Kawahigashi et al.*, 2004]. This likely reflects inputs from modern active-layer soil SOC, as well
104 as previously degraded Holocene permafrost SOC [*Heslop et al.*, 2019], plus further degradation
105 along transport pathways due to long residence time of water in large basins [*Mann et al.*, 2015;
106 *Spencer et al.*, 2015; *Striegl et al.*, 2005]. When permafrost SOC sources are ancient (> 20,000 yr
107 BP) [*Drake et al.*, 2015] and terrestrial thaw process abrupt [*Turetsky et al.*, 2020], stream DOC
108 can become more biologically labile, contributing significantly to in-stream C processing as
109 evidenced by one third to one half of DOC losses in first-order tributaries of the Kolyma River
110 basin [*Mann et al.*, 2015; *Spencer et al.*, 2015; *Vonk et al.*, 2013]. Field observations of soil C
111 has indicated that half of SOC loss is attributable to the lateral flow passing into the aquatic
112 system of the Eight Mile Lake watershed, though the further fate of the transported C is highly
113 uncertain [*Plaza et al.*, 2019]. The need to understand how flow and water exchange regulate the
114 quantity and quality of DOC reaching the stream is also clear from soil column experiments
115 showing substantial (> 70%) C loss in lateral leachate with artificial precipitation [*Zhang et al.*,
116 2017]. Given the uncertainties associated with C cycling in small sized, lower order watersheds
117 [*Raymond and Spencer*, 2015; *Raymond et al.*, 2013], it is useful to examine quantity and quality
118 of DOC along the SOC to stream DOC transport pathways.

119 SOC transport pathways to streams are undergoing profound hydrological changes
120 triggered by permafrost thawing [*Mann et al.*, 2015; *O'Donnell et al.*, 2012]. In Arctic permafrost

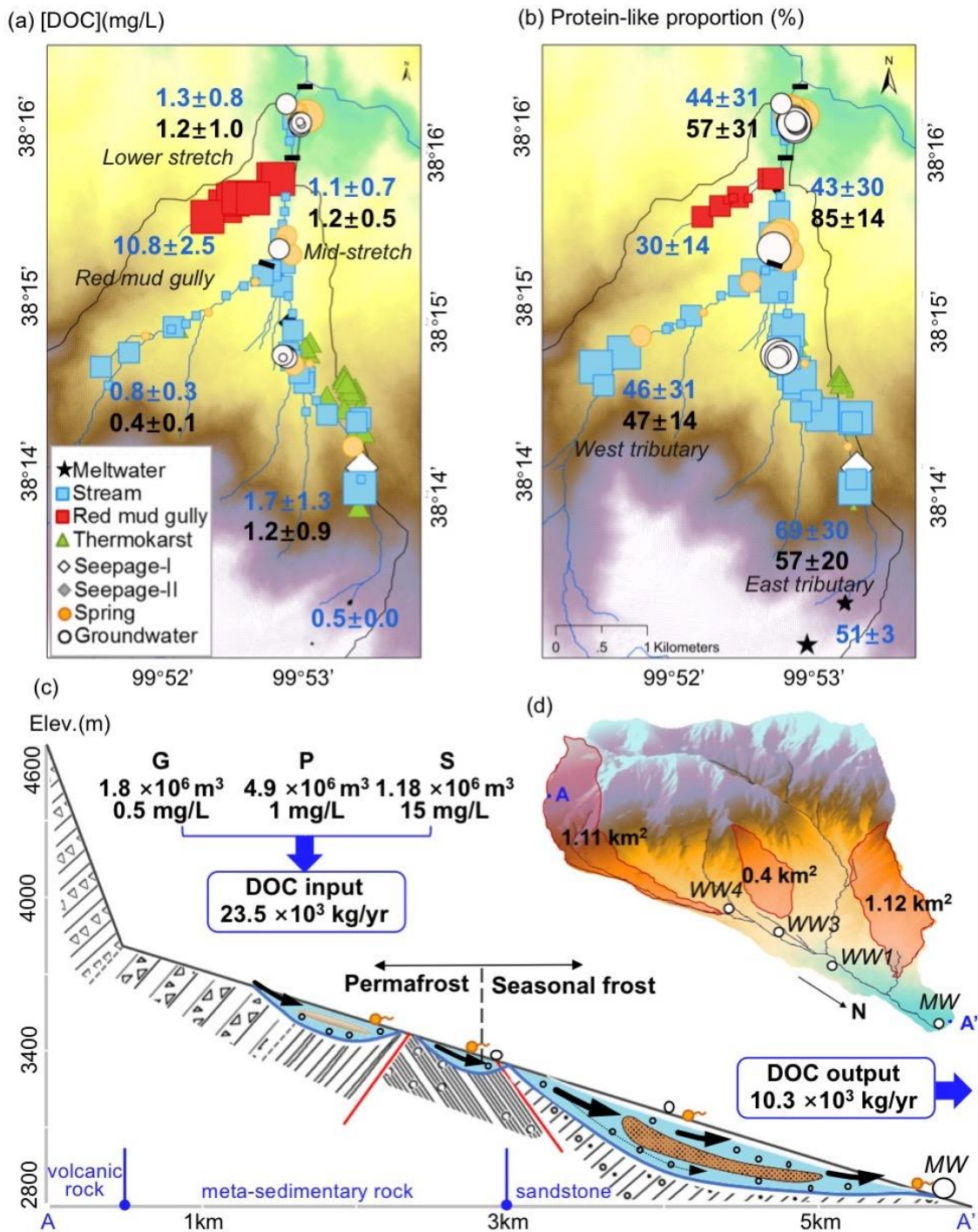
121 areas, there is an increasingly important role of groundwater linked with the increase of base
122 flow and interaction between surface water and groundwater [Connolly *et al.*, 2020; Frey and
123 McClelland, 2009; Vonk *et al.*, 2019]. Observations have identified accelerated input of older
124 DOC exported as baseflow due to the deepening of flow path and increasing discharge [Aiken *et*
125 *al.*, 2014; Barnes *et al.*, 2018; Neff *et al.*, 2006]. Warming is expected to reduce transit time, thus
126 enhancing the propensity for lateral carbon transport along the terrestrial–aquatic continuum
127 [Vonk *et al.*, 2019]. How changing hydrological processes will alter the in-stream C cycling in a
128 warmer future is challenging to disentangle.

129 Assessing complex hydrological processes on catchment scales is a starting point to
130 tackle such challenges. The Qinghai Tibetan Plateau (QTP) is an ideal location to study these
131 processes as it contains the most extensive permafrost cover at the mid- and low- latitudes, but
132 also because the spatially heterogenous degradation of permafrost following the topographical
133 variation also influences hydrology [Cheng and Wu, 2007; Yang *et al.*, 2010]. Increasing
134 precipitation and glacier melting have led to an expansion of water storage ($12.1 \pm 0.6 \text{ Gt yr}^{-1}$)
135 [Yi *et al.*, 2016], especially that of groundwater storage ($5.01 \pm 1.59 \text{ Gt yr}^{-1}$) since 2003 [Zhang
136 *et al.*, 2017]. Given such significant changes in QTP’s hydrological cycle, it is likely that
137 groundwater flow is affected [Ge *et al.*, 2011, Yao *et al.*, 2017], yet few studies have examined
138 such multifaceted changes and its biogeochemical implications. Recent advances in hillslope
139 hydrology, especially the notion of groundwater mean transit time (MTT), defined as the time
140 that water parcels spend between the time entering the unsaturated zone and the time flowing out
141 of the aquifer [Benettin *et al.*, 2015; McDonnell *et al.*, 2010], offer a unique perspective to shed
142 light on DOC processing in northern, alpine permafrost zones. Because MTT is found to range
143 only from days to weeks [Luo and Jiao, 2019], challenging the long-held view that distribution
144 of transit time ranging from years to decades in alpine hillslope hydrological condition [McGuire
145 *et al.*, 2005], this short time scale makes it worthwhile to integrate groundwater into the terrestrial
146 SOC – aquatic DOC continuum. How groundwater – surface water interaction in hillslopes of
147 headwater regions of QTP influences the fate of SOC derived DOC through regulating
148 groundwater transit time, and in turn, the carbon loss in headwaters, remains largely unexplored.

149 To illuminate the emerging and likely significant role that hillslope hydrological
150 processes play in biogeochemical C cycling, this study seeks to shed light on DOC processing in
151 a small (25 km^2), alpine (elevation 2960 to 4820 m a.s.l) watershed named Hulugou (HLGW)

152 located in the northeastern QTP (Fig. 1). The conservative tracers of ^{18}O and electrical
153 conductivity are used in an end-member analysis to ascertain the contribution of frost soil to
154 multiple types of waters and to illustrate the extensive and spatially variable surface water –
155 groundwater interactions in HLGW. The spatial and temporal variations in quantity and quality
156 of dissolved organic matter (DOM) are interpreted to indicate rapid and variable transit time in
157 part caused by changes in groundwater flow paths in response to the freeze-thaw cycle. Finally,
158 how the new constraints on rapid groundwater transit time in the alpine watersheds of the QTP
159 sets the stage for DOC loss in headwaters and its implications for hillslopes acting as DOC
160 processing hotspots are discussed.

161



162

163 **Figure 1.** (a) Concentrations of DOC in eight types of water in HLGW, Qinghai-Tibetan Plateau,
 164 with legends in inserted panel. Small, medium and large symbol sizes indicate low (< 0.7 mg L⁻¹),
 165 medium (0.7-3.6 mg L⁻¹) and high (>3.6 mg L⁻¹) [DOC] according to its tertile values.
 166 Numbers are mean value ± one standard deviation for [DOC] in stream (blue) and subsurface
 167 water (black). (b) Proportions of protein-like component identified by PARAFAC modeling,
 168 with small, medium and large symbol sizes indicating low (<27.4%), medium (27.4–62.4%) and
 169 high (>62.4%) proportions according to tertile values. Numbers are mean value ± one standard

170 deviation for the proportion of protein-like compounds in stream (blue) and subsurface water
171 (black). Maps of Other DOM optical properties SUVA₂₅₄, FI are available in Fig. S1. (c) A
172 schematic diagram of hillslope hydrological process in HLGW for the cross-section A-A' (inset
173 d, three areas of permafrost and seasonal frost in HLGW are shown, with monitoring wells
174 marked in white circles). Water fluxes and [DOC] in three end members (G: glacier-snow melt,
175 P: precipitation, S: frozen soil meltwater) contributing to DOC input are shown. The mass
176 balance of DOC input and out fluxes suggests that about half of DOC is processed in HLGW.
177
178

179 **2 Material and Methods**

180 **2.1 Study Area and Sample Collection**

181 The study was conducted in Hulugou watershed (HLGW), upper Heihe basin, NE
182 Qinghai-Tibetan Plateau (99°50' – 99°54' E, 38°12' – 38°17' N; 2960 to 4820 m a.s.l, 25 km²).
183 The HLGW consists of three geomorphic units of glacier-snow covered mountain, rocky hills,
184 and meadow steppe. Glacier, permafrost and seasonal frost ground have experienced
185 degradation, albeit to different extent within the HLGW [Li *et al.*, 2014]. A first-order stream
186 network with extensive surface water and groundwater exchanges [Chang *et al.*, 2018; Evans *et*
187 *al.*, 2015] is superimposed on permafrost (3400 m to 4500 m a.s.l) with abundant thermokarst
188 ponds, seasonal frost ground (2900 m to 3400 m a.s.l), and degraded permafrost (3450 m to 3600
189 m a.s.l) with erosional channels (Fig. 1).

190 Water samples (n=129) were collected from HLGW for a total of five times in July 2012
191 (n=22), April (n=11), July (n=28) and September 2013 (n=30), and September 2018 (n=38),
192 respectively. Eight types of water were sampled, including glacier-snow melt, streams, a thermo-
193 erosional red mud gully, thermokarst ponds, seepage-I, seepage-II, spring and groundwater, with
194 detailed sampling locations described in Table 1. All types of water samples except groundwater
195 were collected from 2 cm below the surface. The meltwater sample was collected in triplicate at
196 the same time from melting glacier-snow in bare gravel zone, and analyzed individually, with
197 results reported as mean values of the triplicate samples that represent this one type of water. The
198 upper-stretch of the stream network in HLGW includes the east and the west tributaries
199 originating at elevation above 4765 m. After the east and the west tributaries converge, the mid-
200 stretch flows through the permafrost zone into the seasonal frozen soil zones, and becomes the
201 lower-stretch after the red mud gully joins in (Fig. 1). Red mud gully is an erosional tributary;
202 formed by water cutting deeply into the seasonal frost ground in the alpine meadow between

203 3300 m to 3000 m a.s.l, and thus classified separately as a type of water. Thawing of permafrost
204 results in many small thermokarst ponds (diameter < 1 m mostly), observed in the alpine meadow
205 at an altitude ranging from 3351 m to 3548 m close to the east tributary. The aquifer lithology
206 and the installation of the observation wells are described in a previous study [Hu *et al.*, 2019].
207 Groundwater samples were collected from the wells shown in Fig. 1d with well depths being
208 WW1–25 m, WW3–5 m, WW3–10 m, WW3–20 m, WW3–30 m and MW–30 m (Fig. 1d), after
209 the wells have been primed until stable readings of temperature and EC were reached.

210 Cation and anion samples were filtered with 0.22 μm nylon filters. Stable isotopes H_2^{18}O
211 and D_2O samples were filtered with 0.22 μm nylon filters into 2 ml glass bottles then immediately
212 sealed without head space. Dissolved organic matter (DOM) samples were filtered using glass
213 fiber syringe filters (Whatman GF/F style) with a 0.7 μm nominal pore size into pre-combusted
214 (at 450 $^\circ\text{C}$ for 6 hours) 22 ml brown glass bottles and crimp sealed with Teflon-faced silicone
215 septa. All samples were filtered immediately after sampling and stored on ice at 4 $^\circ\text{C}$ for shipment
216 to laboratory.

217

218 **2.2 Measurements of field and chemical parameters, stable isotopes and DOM**

219 Temperature (T), electrical conductivity (EC), pH and alkalinity were measured in the
220 field. Stable isotopes (δD and $\delta^{18}\text{O}$) were measured on a water isotope spectrometer analyzer
221 (Model PICARRO L2130-I) at Pri-ecoco, Beijing, China (see Text S1 of Supporting
222 Information). Major anions and cations of samples in 2012 and 2013, were measured by ion
223 chromatography (IC-1000, Dionex) and Inductively Coupled Plasma Atomic Emission
224 Spectroscopy (ICPAES, Teledyne Leeman, Prodigy), respectively. Major ions of sample in 2018
225 were measured on IC (Aquion, Dionex) with CS18 analytical column for anions, and CS16
226 column for cations, respectively. DOC concentrations of all water samples and soil extraction
227 solutions (see Text S2 and Fig. S2 of Supporting Information on soil incubation) were measured
228 on a Shimadzu TOC Analyzer. Detailed procedures are in Text S1 of Supporting Information.

229 Absorbance of UV-Visible chromophore DOM (CDOM) was measured by a UV-Visible
230 Spectrophotometer (Agilent 8453) scanning from 200 to 800 nm (1 nm increments) to acquire
231 absorbance for samples collected in 2012 and 2013. Prior to analyzing samples, a quartz cuvette
232 filled with Milli-Q water was used to establish a daily baseline. Excitation emission matrices

233 (EEMs) were employed by scanning over an excitation (ex) range of 240 to 450 nm at 10 nm
234 increments, and an emission (em) range of 350 to 550 nm at 2nm increments on a JY-Horiba
235 Fluoromax-3 spectrofluorometer (Queens College, CUNY) with instrument-specific corrections,
236 Raman normalization, inner filter correction, and cuvette blank subtraction applied. Optical
237 properties of samples collected in 2018 were analyzed using a Horiba Aqualog
238 spectrofluorometer (Southern University of Science and Technology) following the same
239 procedure. EEMs were generated over excitation wavelengths between 246.58 to 827.57 nm in
240 about 1.2-nm interval and emission wavelengths between 220 to 800 nm in 1-nm interval. All
241 DOM measurements were completed within two weeks of sampling.

242 To correct for minor effect of light scattering by particles and microbubbles, wavelength-
243 independent correction is conducted by subtracting the mean absorbance at range of 600 to 800
244 nm from all spectral absorbance values [*Green and Blough, 1994*]. Specific UV absorbance
245 (SUVA) represents relative DOM aromaticity [*Weishaar et al., 2003*], and SUVA at 254 nm
246 (SUVA₂₅₄) was applied in this study following previously reported methods [*Weishaar et al.,*
247 *2003*]. Fluorescence index (FI) is calculated as the ratio of intensities emitted at 470 nm and 520
248 nm at an excitation wavelength of 370nm, with lower value (~1.2) usually indicating for more
249 terrestrial derived DOM and higher (~1.8) for more microbial DOM sources [*Cory and*
250 *McKnight, 2005; McKnight et al., 2001*]. Freshness index (BIX) is calculated as the ratio of
251 emission intensity at 380 nm to the maximum intensity between 420 nm and 435 nm at an
252 excitation wavelength of 310 nm [*Parlanti et al., 2000*]. Higher value of BIX represents a higher
253 proportion of fresh DOM [*Parlanti et al., 2000*].

254 **Table 1.** Description of water types, electrical conductivity (EC), isotopic compositions, DOC concentration and optical properties in
 255 eight types of water in HLGW sampled between 2012-2018.
 256

Description	Elevation range (m)	Types of water in HLGW	n	EC ($\mu\text{s cm}^{-1}$)	$\delta^{18}\text{O}$ (‰)	δD (‰)	DOC (mg L^{-1})	Protein proportion (%)	SUVA ₂₅₄ ($\text{L mgC}^{-1} \text{m}^{-1}$)	FI	BIX
Melting glacier-snow in bare gravel zone	4100	Meltwater	1	179±1	-10.6±0.5	-64.8±3.8	0.5±0.0	51±3	0.33±0.17	1.94±0.04	0.83±0.02
Upper-, mid-, and lower-stretch *	3620-2920	Stream	41	355±141	-9.1±0.4	-52.1±4.6	1.3±1.1	56±33	1.09±0.63	1.62±0.16	0.73±0.14
Erosional tributary cutting through the seasonal frost zone	3200-3050	Red mud gully	10	2881±399	-6.3±0.4	-32.8±2.5	10.8±2.5	30±14	2.84±0.78	1.50±0.14	0.71±0.09
Seasonal frost ground in alpine meadow	3620-3350	Thermokarst ponds	26	334±123	-4.5±0.7	-24.8±5.3	14.3±3.3	24±11	3.75±0.48	1.37±0.09	0.59±0.05
Emerging thermokarst	3610	Seepage-I	2	322±25	-6.4±0.1	-37.1±0.6	7.1±1.0	45±22	3.16±0.35	1.29±0.04	0.58±0.03
Slow discharging spring	3410-3060	Seepage-II	4	501±181	-9.1±0.4	-52.2±2.0	1.5±0.8	43±39	1.16±0.80	1.60±0.16	0.61±0.12
Fast discharging spring	3570-2950	Spring	17	450±196	-8.7±0.3	-50.1±2.2	1.1±1.0	59±31	1.14±0.60	1.75±0.21	0.74±0.21
Six wells‡	3300-2970	Groundwater	13	573±61	-8.5±0.3	-48.0±2.1	1.0±0.4	62±24	0.88±0.45	1.82±0.14	1.12±0.38

257 * Upper-stretch includes east and west tributaries and is in permafrost zone, mid-stretch is in seasonal frost zone, and the lower-stretch is in seasonal frost
 258 zone

259 ‡ Wells shown in Fig. 1d with depths being WW1–25 m, WW3–5 m, WW3–10 m, WW3–20 m, WW3–30 m and MW–30

260 **2.3 Parallel Factor Analysis (PARAFAC) of DOM Fluorescence Spectra**

261 Fluorescence spectra, obtained as EEMs, are used to quantify the contribution of
262 fluorescent DOM components through PARAFAC modeling [Coble, 1996; Murphy *et al.*, 2013].
263 PARAFAC was conducted following the procedures described in a previous algorithm to
264 quantify the protein-like fluorophores and humic-like substances of DOM [Murphy *et al.*, 2013;
265 Stedmon and Bro, 2008]. Prior to outlier tests, the intensity of EEMs of samples in 2018 was
266 linearly interpolated to match the emission ranging 250 to 450 nm at an interval of 10 nm and
267 excitation ranging 300 to 550 nm at an interval of 2 nm. To avoid highly fluorescent samples
268 exerting significant leverages on the PARAFAC model, normalization of each EEM to its
269 integrated fluorescence was applied before model fitting [Murphy *et al.*, 2013]. Normalized
270 fluorescence of each EEM was reversed to its raw fluorescence after model fitting.

271 We applied two PARAFAC models with two datasets. The first model includes all 100
272 water samples and the second adds 47 soil extracted samples to the first dataset of 100 water
273 samples (see Section 2.7 on soil extraction). A series of three to six component- models were
274 fitted to the dataset, with non-negativity constraint of 10^{-8} applied to each. The split-half
275 validation was achieved through splitting the data in half and modeling each half separately,
276 fitting 20 models with random starts, and by inspection towards lowest residuals [Murphy *et al.*,
277 2013]. The PARAFAC analysis resolved a four-components model comprising the EEMs
278 dataset, explaining 97.8% of the total variance. The comparisons of two model exports are shown
279 in Figure S6, suggesting consistency with additional samples. Spectra loadings of both excitation
280 and emission mode for each component were matched to the OpenFluor database
281 (<https://openfluor.lablicate.com/of/measurement/1104>), and the description of each component
282 was interpreted from matched compounds identified from previous studies with similarity >95%
283 [Murphy *et al.*, 2014]. The identified four fluorescence components (C1 to C4) are ubiquitous
284 and common in marine environments [Catala *et al.*, 2015; Wunsch *et al.*, 2018], as well as
285 cryosphere such as Arctic surface waters [Gonçalvesaraujo *et al.*, 2016] and ice cores in Arctic
286 Canada [Brogi *et al.*, 2018], and ice in the Antarctic seas [Stedmon *et al.*, 2011]. The C1 and C3
287 components have a broader emission spectrum and two extraction spectra peaks, traditionally
288 referred to as humic-like components (Fig. S3). The C2 (ex: 270 nm; em: 304 nm) and C4 (ex:
289 290 nm; em: 338) components have narrower spectra with excitation and emission maxima

290 below 350 nm (Fig. S3), and are similar to the spectra of tyrosine and tryptophan, respectively
 291 [Murphy *et al.*, 2008]. The characterization of C2 and C4 represents amino-acids, free or bound
 292 in proteins compounds. The proportion of protein-like fluorophores is calculated as the sum of
 293 C2 and C4 intensities divided by the bulk intensity of the sample. Representative EEMs of
 294 different water types are enclosed in Supporting Information (Figs. S4 and S5).

295

296 **2.4 End Member Analysis Based on Conservative Tracers**

297 A three end-member mixing analysis constrained by conservative tracers $\delta^{18}\text{O}$ and EC
 298 was used to calculate the fractions of glacier-snow (f_G), precipitation (f_P) and frozen soil melt
 299 water (f_S) contributing to stream and subsurface waters in HLGW. The same three end members
 300 have been adopted in a hydrograph separation study of HLGW [Li *et al.*, 2014]. The analysis is
 301 based on the following assumptions: (1) the three water sources are the dominant sources over
 302 the ablation season and that any other sources are negligible; (2) shallow, organic layer of frozen
 303 soil is involved in lateral flow thus provides a signature needing representation.

$$304 \quad f_G \times C_G^{18O} + f_P \times C_P^{18O} + f_S \times C_S^{18O} = C_i^{18O} \quad (1)$$

$$305 \quad f_G \times C_G^{EC} + f_P \times C_P^{EC} + f_S \times C_S^{EC} = C_i^{EC} \quad (2)$$

$$306 \quad f_G + f_P + f_S = 1 \quad (3)$$

307 where f represents the estimated fraction of a given endmember contributing to the
 308 specific sample i ; the subscripts G , P and S represent the glacier-snow meltwater, precipitation
 309 and soil endmember, respectively; C^{18O} and C^{EC} represent the $\delta^{18}\text{O}$ and EC of the sample
 310 specified in the subscript, respectively.

311 The $\delta^{18}\text{O}$ and EC values to constrain the glacier-snow endmember composition rely on
 312 not only a meltwater sample collected in triplicate and analyzed individually in this study, but
 313 also two newly deposit snow samples collected in May and November of 2012 and one meltwater
 314 sample collected in July 2012 in the front of a glacier in HLGW [Li *et al.*, 2015] (Table 2). The
 315 elevation-weighted $\delta^{18}\text{O}$ (-7.66‰) and the volume-weighted $\delta^{18}\text{O}$ (-7.7‰) are comparable based
 316 on 65 rainwater samples collected weekly between June 28 to Sept 2, 2012 from 7 elevations
 317 (2960 to 4160 m a.s.l.) of the HLGW [Chang *et al.*, 2018]. The volume-weighted $\delta^{18}\text{O}$ becomes
 318 more negative with higher elevation at a rate of 0.19‰ per 100 m in HLGW [Chang *et al.*, 2018].
 319 The volume-weighted mean EC and $\delta^{18}\text{O}$ are used to represent the precipitation endmember

320 (Table 2). In July 2013, pore waters were collected from piezometer installed to depths of 0.6 m
 321 to 1.5 m; groundwater was collected from monitoring well WW4 with a depth of 1 m. These 3
 322 samples were regarded to represent frozen soil water [Li *et al.*, 2014; Ma *et al.*, 2017]. The EC
 323 and $\delta^{18}\text{O}$ endmember compositions were averaged from these samples plus 87 samples collected
 324 underneath 7 soil profiles at elevation between 3620 to 2920 m analyzed similarly in Li *et al* [Li
 325 *et al.*, 2014] (Table 2).

326 To estimate the uncertainty associated with the tracer-based end-member analysis, a
 327 classical Gaussian error propagation equation was employed [Genereux, 1998]. The calculation
 328 followed procedure described elsewhere [Chang *et al.*, 2018]. The fractions and associated
 329 uncertainties are reported in Table 2 and Table S1.

$$330 \quad W_f = \left[\left(\frac{\partial f}{\partial C_G^{18\text{O}}} W_G^{18\text{O}} \right)^2 + \left(\frac{\partial f}{\partial C_P^{18\text{O}}} W_P^{18\text{O}} \right)^2 + \left(\frac{\partial f}{\partial C_S^{18\text{O}}} W_S^{18\text{O}} \right)^2 + \left(\frac{\partial f}{\partial C_i^{18\text{O}}} W_i^{18\text{O}} \right)^2 + \left(\frac{\partial f}{\partial C_G^{\text{EC}}} W_G^{\text{EC}} \right)^2 + \right. \\ 331 \quad \left. \left(\frac{\partial f}{\partial C_P^{\text{EC}}} W_P^{\text{EC}} \right)^2 + \left(\frac{\partial f}{\partial C_S^{\text{EC}}} W_S^{\text{EC}} \right)^2 + \left(\frac{\partial f}{\partial C_i^{\text{EC}}} W_i^{\text{EC}} \right)^2 \right]^{1/2} \quad (4)$$

332 where W represents the uncertainty in the variable specified in the subscript, i.e W_f
 333 represents the uncertainty of the contribution fraction for a given end member in a sample, $W_G^{18\text{O}}$
 334 represents the uncertainty of $\delta^{18}\text{O}$ in glacier-snow endmember.

335

336 **2.5 Estimation of DOC Loss: ΔDOC**

337 Because DOC is non-conservative, we first estimate an initial DOC (DOC_0) through
 338 summation of DOC contributed from each endmember (equation 5).

$$339 \quad \text{DOC}_0 = f_G \times \text{DOC}_G + f_P \times \text{DOC}_P + f_S \times \text{DOC}_S \quad (5)$$

340 The DOC concentration ($0.5 \pm 0.02 \text{ mg L}^{-1}$) in meltwater at the highest elevation is taken
 341 to represent the glacier-snow endmember (Table 2). The DOC concentration ($15 \pm 2.5 \text{ mg L}^{-1}$)
 342 of pore water samples collected by piezometers is taken to represent the soil endmember (Table
 343 2). Though DOC of rainfall was not measured in HLGW, the volume-weighted mean DOC is
 344 0.9 mg L^{-1} in three remote meteorological stations and $1.1 \pm 0.5 \text{ mg L}^{-1}$ in Lhasa city of central
 345 QTP [Li *et al.*, 2017; Li *et al.*, 2018]. The DOC of 1.0 mg L^{-1} is taken to represent the precipitation
 346 endmember (Table 2).

347 The difference between initial DOC and measured DOC of a sample suggests the loss of
 348 carbon along the flow path of water to the sampling point. The DOC loss (ΔDOC) is calculated
 349 by subtracting measured DOC concentration ($[\text{DOC}]$) of a given water sample from its initial
 350 DOC (DOC_0) calculated above, where larger ΔDOC corresponds to more loss of DOC during
 351 transport.

$$352 \quad \Delta\text{DOC} = \text{DOC}_0 - [\text{DOC}] \quad (6)$$

353
 354 **Table 2.** Mean and standard deviation (mean \pm std) of $\delta^{18}\text{O}$ (‰) and electrical conductivity (EC,
 355 $\mu\text{S}/\text{cm}$) used in computing end-member mixing fractions and their uncertainties (W), and DOC
 356 (mg/L) in the three end members.

End-member	$\delta^{18}\text{O}$ (‰)				EC ($\mu\text{S}/\text{cm}$)				DOC (mg/L)
	mean \pm std	n	t^* (0.7)	$W^{18\text{o}}$ (0.7)	mean \pm std	n	t^* (0.7)	W^{EC} (0.7)	mean \pm std
Glacier-snow meltwater	-14 ± 3.9	6	1	3.9	160 ± 27	4	1	27	0.5 ± 0.02
Precipitation	-7.7 ± 2.0	65	0.85	1.7	35 ± 3.0	65	0.85	2.5	1
Frozen soil meltwater	-5.3 ± 0.2	3	1	0.2	3487 ± 542	4 [‡]	1	542	15 ± 2.5

357 * The uncertainty of each tracer in a specific endmember is calculated as the standard deviation
 358 multiplying the t value under coefficient level at 0.7.

359 ‡ The mean value of EC is averaged from three endmember samples and the average EC value of 87 soil
 360 samples from Li et al., [2004].

361

362 2.6 Estimation of Groundwater Mean Transit Time

363 First order kinetics have been widely used to describe biodegradation of DOC incubation
 364 experiments [Catala et al., 2015], allowing for calculation of the degradation rate constant (λ) as
 365 in equations (7), where the DOC_0 usually represents the starting point of the experiment.

$$366 \quad \text{DOC} = \text{DOC}_0 \times e^{-\lambda t} \quad (7)$$

367 Because photodegradation is unlikely in subsurface environment, the biodegradation rate
 368 constant is assumed to regulate DOC degradation in groundwater. Re-arranging equation (7) to
 369 simulate the ΔDOC change in groundwater observed at the outlet of HLGW in July and
 370 September result in equation (8), with the calculated time, t , regarded as representing
 371 groundwater mean transit time (MTT). The assumptions for the linkage between DOC loss
 372 behavior and transit time are (1) photodegradation is negligible in subsurface environment; (2)

373 the potential direct input from particle organic carbon along the pathway is excluded because
374 particles would not be transported by groundwater; (3) physical removal of DOC due to
375 retardation is expected to be fast, evenly distributed and hence not considered.

$$376 \quad 1 - \Delta DOC / DOC_0 = e^{-\lambda_{gw}t} \quad (8)$$

$$377 \quad MTT \approx t = -\frac{\ln(1 - \Delta DOC / DOC_0)}{\lambda_{gw}} \quad (9)$$

378 where λ_{gw} represents DOC degradation constant in groundwater which has been corrected
379 to observed groundwater temperature of 5 °C based on the Arrhenius equation [Catalan *et al.*,
380 2016] from the incubation experiment temperature of 20 °C.

381

382 **2.7 Soil Incubation Experiment**

383 A batch incubation experiment of SOC was initiated in the field to minimize sample
384 storage artifacts. Four soil profiles were sampled at elevations from 2850 to 3600 m a.s.l and
385 included seasonal frozen soil, thermokarst ponds and less degraded permafrost soil (Table S2).
386 Approximately 5 g of soil was weighed and added to pre-combusted 20-ml glass bottles in
387 triplicate, and filled with 15 – 19 ml Milli-Q water. Then the bottles were crimp sealed with
388 Teflon-coated septa and aluminum cap right away. The bottles were stored in room temperature
389 in dark before the supernatant was sampled at day 1, 3 and 40, sacrificing a bottle at a sampling
390 time. The supernatant was filtered and measured for DOC concentrations, UV-visible absorbance
391 and fluorescence spectra were performed within a week of sampling following the same protocol
392 as in section 2.2.

393 A second incubation experiment used a reactor approach similar to Drake *et al* to evaluate
394 the biodegradation rate of soil derived DOC [Drake *et al.*, 2015] (Fig. S2). The shallow frost
395 sample was collected by excavation to reach a depth of 50 cm within the active layer with
396 thickness of 2 m nearby the well WW4. The sample was kept and transported on ice in a cooler
397 to the lab. The details of incubation set up and sampling were described in Text S2 of supporting
398 information.

399

400

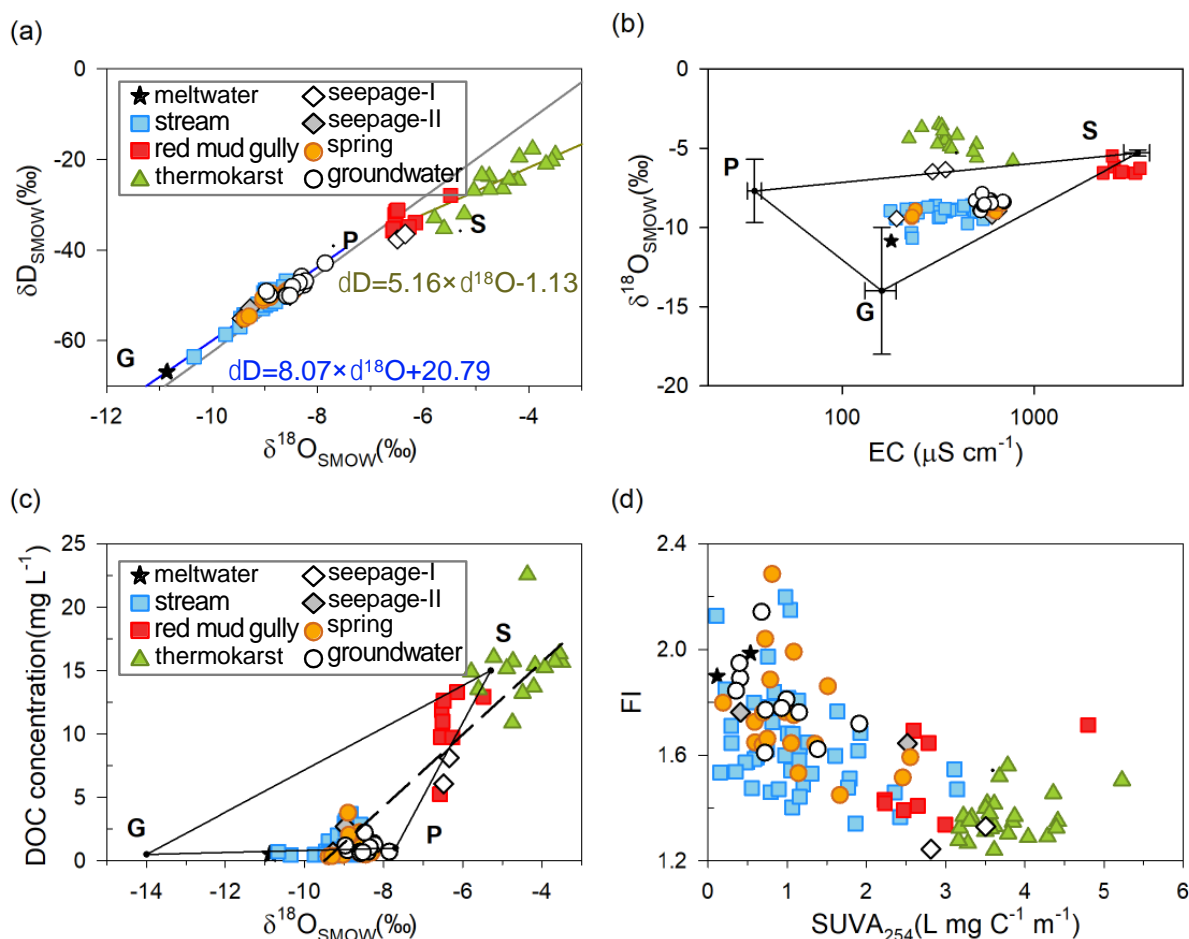
401 **3 Results**

402 **3.1 Frozen Soil Meltwater Contributes to All Water Types**

403 Stable isotope characteristics of eight types of water indicate the influence of not only
404 glacier-snow meltwater (G) and precipitation (P) but also frozen soil melt water (S) endmembers
405 (Figs. 2a and 2b). Stream and subsurface water (groundwater, spring and seepage-II) samples
406 fall within the triangle defined by the G, P and S endmembers (Figs. 2a and 2b). The regression
407 line of meltwater, stream, seepage-II, spring and groundwater ($8.07 \times \delta^{18}\text{O} + 20.79$, $r^2=0.92$,
408 $n=71$, blue line in Fig. 2a) is similar to the local meteoric water line (LMWL: $8.5 \times \delta^{18}\text{O} + 22.6$,
409 gray line in Fig. 2a) of HLGW [Ma *et al.*, 2017]. In contrast, thermokarst pond waters, two
410 seepage-I samples and red mud gully waters exhibit more positive isotopic compositions and fall
411 below the local meteoric water line (LMWL) on a different trend line ($5.16 \times \delta^{18}\text{O} - 1.13$,
412 $r^2=0.83$, $n=20$, black line in Fig. 2a), indicating fractionation due to evaporation [Froehlich *et*
413 *al.*, 2008]. The red mud gully waters are most similar to the frozen soil melt water endmember
414 in compositions (Fig. 2b); and this is interpreted to indicate that red mud gully waters are derived
415 from the frozen soil melt water. The two seepage-I samples (emerging thermokarst) represent
416 mixing between roughly $25\% \pm 1\%$ of the soil endmember, and $75\% \pm 1\%$ of the precipitation
417 endmember, respectively (Fig. 2b). The thermokarst pond waters are also likely a mixture of the
418 S and P endmembers, although the $\delta^{18}\text{O}$ values have become more positive due to evaporation.
419 In summary, red mud gully, emerging thermokarst (seepage-I) and thermokarst ponds all have
420 significant frozen soil meltwater contribution.

421 Using EC and $\delta^{18}\text{O}$ to un-mix among the three endmembers for stream and subsurface
422 water (groundwater, spring, and seepage-II) samples falling within the triangle, precipitation
423 contributes on average about $62\% \pm 7\%$, $64\% \pm 4\%$, $61\% \pm 4\%$ and 63% of the water in stream,
424 groundwater, spring, and seepage-II, respectively (Fig. 2b). Glacier-snow meltwater ranked
425 second for stream ($28\% \pm 6\%$), groundwater ($18\% \pm 4\%$) spring ($24\% \pm 4\%$) and seepage-II (26%)
426 contributions. Frozen soil meltwater contributed the least to the stream waters ($10\% \pm 4\%$), but
427 contributed 11% , $15\% \pm 5\%$, and $17\% \pm 2\%$ in seepage-II, spring, and groundwater samples,
428 respectively.

429



430

431 **Figure 2.** (a) Stable isotope compositions ($\delta^{18}O$ and δD) of eight types of water in HLGW. Three
 432 endmembers: glacier-snow meltwater (G), precipitation (P) and frozen soil meltwater (S) are
 433 marked according to their compositions. Local meteoric water line (LMWL: $8.5 \times \delta^{18}O + 22.6$)
 434 is shown as a gray line [Ma et al., 2017]. (b) The $\delta^{18}O$ vs electrical conductivity (EC, log scale)
 435 of eight types of water samples from HLGW. The triangle outlines the three end members with
 436 the error bar representing standard deviation for the two tracers. Uncertainties in $\delta^{18}O$ and EC of
 437 the three endmembers are reported in Table 2. (c) The $\delta^{18}O$ vs DOC concentrations for all eight
 438 types of water within HLGW are shown with a positive correlation ($p < 0.01$; $n = 103$). The
 439 triangle outlines the three end members according to their $\delta^{18}O$ and DOC concentrations. (d) The
 440 $SUVA_{254}$ vs FI for all eight types of water with a negative correlation ($r = -0.59$, $p = 0.01$).

441

442 3.2 Frozen Soil Thaw Supplies the Majority of DOM to Surface and Subsurface Waters

443 Several lines of evidence suggest that DOM in surface water has been influenced by
 444 DOM from thawing of seasonal frost and/or permafrost. Three types of water show high DOC
 445 levels (Table 1): thermokarst ponds ($14.3 \pm 3.3 mg L^{-1}$), red mud gully ($10.8 \pm 2.5 mg L^{-1}$) and
 446 seepage-I ($7.1 \pm 1.4 mg L^{-1}$). The elevated DOC levels of these three types of water are consistent

447 with the large contribution of frozen soil melt water endmember (Fig. 2b). These waters also
448 show the most positive $\delta^{18}\text{O}$, with a correlation with DOC concentrations (Fig. 2c). Because
449 DOC concentrations in glacier-snow melt (0.5 mg L^{-1}) and precipitation (1 mg L^{-1}) endmembers
450 are low, this means that DOC in the stream ($1.3 \pm 1.1 \text{ mg L}^{-1}$, spring ($1.1 \pm 1.1 \text{ mg L}^{-1}$),
451 groundwater ($1.1 \pm 0.4 \text{ mg L}^{-1}$) and seepage-II ($1.5 \pm 0.8 \text{ mg L}^{-1}$) must include a source from
452 thawing of frozen soil, consistent with the water source analysis results above. When the DOC
453 concentrations of all samples are divided according to the two tertile values, with one third of
454 samples each belonging to low, medium and high levels equally (Fig. 1a), stream waters ($n = 29$)
455 with low DOC level ($0.7 \pm 0.3 \text{ mg L}^{-1}$) display the most negative $\delta^{18}\text{O}$ values of $-9.20 \pm 0.48 \text{ ‰}$
456 while stream waters ($n = 12$) with medium DOC level ($2.9 \pm 0.7 \text{ mg L}^{-1}$) show in-between $\delta^{18}\text{O}$
457 of $-8.82 \pm 0.14 \text{ ‰}$, indicating input of frozen soil-derived DOC to streams.

458 Further support for the importance of thawing supplied DOM in the watershed is based
459 on characterization of the quality of DOM by UV-visible and fluorescence spectroscopy because
460 of its ability to absorb light and fluoresce. The optical properties including SUVA_{254} , FI and BIX
461 all point to various degrees of influence by DOM from thawing of seasonal frost and/or
462 permafrost soil. Thermokarst, red mud gully and seepage-I (emerging thermokarst) waters
463 characterized by elevated DOC concentration display the highest SUVA_{254} and the lowest FI
464 values (Fig. 2d and Table 1). This indicates overwhelming influence by terrestrial plant-soil
465 sourced DOM with high aromaticity from organic matter produced some time ago. The glacier-
466 snow meltwater is the least likely to be influenced by any DOM from frozen soil melt, and thus
467 shows the lowest SUVA_{254} ($0.33 \pm 0.17 \text{ L mgC}^{-1} \text{ m}^{-1}$) and the highest FI (1.94 ± 0.04). Stream,
468 spring and groundwater display SUVA_{254} and FI values between the aforementioned two DOM
469 optical “endmembers” (Fig. 2d). Subsurface waters (spring and groundwater) show higher BIX
470 and FI values than stream water, indicating recent microbially processed DOM [Parlanti *et al.*,
471 2000], consistent with the interaction with microbes in subsurface environment. The BIX values
472 of meltwater, groundwater, and most spring water lie above the median BIX value of 0.69 of the
473 all eight types of water, while those of most stream, red mud gully, seepage-I and thermokarst
474 pond waters are below (Fig. S6).

475

476 3.3 Differences in DOM Quality in Surface and Subsurface Waters Support Subsurface 477 Processing

478 The DOM of meltwater collected at the origin of the east tributary displays low SUVA₂₅₄
479 of $0.33 \pm 0.17 \text{ L mg C}^{-1} \text{ m}^{-1}$ and $51 \pm 3\%$ of protein-like fluorophores based on a four-component
480 PARAFAC model quantifying fluorescent DOM composition (Figs. 1b and Table 1). These
481 values are comparable to that of glacier-snow meltwater ($n=2$) in southwest QTP, with SUVA₂₅₄
482 of $0.60 \text{ L mg C}^{-1} \text{ m}^{-1}$ and $>50\%$ of amino-acids [Spencer *et al.*, 2014; Xu *et al.*, 2013]. Although
483 the meltwater can be a source of bioavailable DOC based on FT-ICR-MS analysis with high
484 proportions of protein-like fluorophores [Feng *et al.*, 2016], its DOC concentration is also the
485 lowest among the eight types of water. Thus, there must be additional DOC with such optical
486 properties from other sources. Three types of water with significant S contribution, including
487 thermokarst, red mud gully and seepage-I, contain high DOC with substantial (though variable)
488 proportions of protein-like fluorophores of $24 \pm 11\%$ ($n=12$), $30 \pm 14\%$ ($n=8$), and $45 \pm 22\%$ ($n=2$),
489 respectively (Table 3). The permafrost SOC fingerprints evident in these three types of water are
490 also observed in stream, spring and groundwater with DOM containing substantial though
491 spatially variable proportions of protein-like fluorophores (Fig. 1b), intermediate SUVA₂₅₄ of \sim
492 $1 \text{ L mg C}^{-1} \text{ m}^{-1}$ and medium-to-high FI of > 1.6 (Fig. S6).

493 Several lines of evidence support that differences in water – permafrost soil hydrological
494 interactions in the upper-, mid-, and lower-stretches of the HLGW lead to spatial variations in
495 DOM quality in surface and subsurface waters. In the upper-stretch, the quantity and quality of
496 DOC in surface water exhibit notable differences between the east and the west tributaries.
497 Concentrations of DOC and proportions of protein-like components are on average higher in the
498 east tributary ($1.7 \pm 1.3 \text{ mg L}^{-1}$, $69 \pm 30\%$) that drains two areas of permafrost and seasonal frost
499 areas than those in the west tributary ($0.8 \pm 0.3 \text{ mg L}^{-1}$, $46 \pm 31\%$) that drains only one smaller area
500 of permafrost (Fig. 1d and Table 3). Subsurface waters of the upper stretch display lower DOC
501 concentration than surface water (Fig. 1a), with slightly less protein-like proportions and higher
502 SUVA₂₅₄ (Fig. 1b and Table 3).

503 From the mid-stretch to the outlet of the HLGW, the quality of stream DOC reflects
504 mixing of upstream waters from the east and west tributaries, and after convergence of red mud
505 gully, with this additional input (Fig. 1a and Table 1). The comparable subsurface water DOC

506 mean concentrations between the upper-stretch east tributary (1.2 ± 0.9 mg L⁻¹) and lower-
 507 (1.2 ± 1.0 mg L⁻¹) stretches (Table 3) suggests that a groundwater flow path may connect the
 508 highest elevation area in the east with the lowest elevation area (Figs. 1a and 1b). The mid-stretch
 509 subsurface water may have been influenced more by a cluster of thermokarst ponds nearby
 510 because the proportion of protein-like fluorophores (85 ± 14 %, n=4) in four subsurface water
 511 samples from the mid-stretch nearly double that of stream water, with higher SUVA₂₅₄ values as
 512 well (Fig. 1b and Table 3). This may be attributed to less photodegradation of permafrost sourced
 513 DOM in subsurface environment than in surface water.

514 In each stretch of the HLGW stream network, the mean value of FI in subsurface waters
 515 is substantially higher than that in the surface waters (Table 3), indicating more microbially
 516 processed DOM in subsurface environment, except for the mid-stretch where subsurface
 517 processing may be weak. When protein-like proportion is divided into three groups again
 518 according to the two tertile values, all of 12 groundwater samples, and 10 out of 13 spring
 519 samples belong to medium and high levels (Fig. 1b). The spring waters also have the highest
 520 bulk fluorescence intensity averaging 3.85 ± 6.58 RU (Dataset S1). Taken together, the
 521 differences in DOM quality in surface and subsurface waters, along with the spatially variable
 522 distribution of optical properties of DOM, suggest that subsurface environment actively
 523 participate in DOM processing in headwaters of the QTP, with microbially driven biodegradation
 524 likely being important (see section 4.1).

525

526 **Table 3.** DOC concentrations, optical properties of DOM, proportions of glacier-snow (f_G),
 527 precipitation (f_P) and soil water (f_S) contributing to stream and subsurface waters and associated
 528 DOC loss for the upper, mid and lower stretches of HLGW.

Category	Type*	n	DOC (mg/L)	Protein proportion (%)	SUVA ₂₅₄ (L mg C ⁻¹ m ⁻¹)	FI	f_G	f_P	f_S	DOC ₀ (mg/L)	ΔDOC (mg/L)
Upper stretch: east tributary (3620-3190 m)	surface	21	1.7±1.3	69±30%	1.18±0.60	1.60±0.14	29±9%	62±9%	10±4%	2.2±0.6	1.2±0.8
	subsurface	9	1.2±0.9	57±20%	1.38±0.73	1.71±0.11	19±2%	64±4%	17±2%	3.3±0.3	2.3±0.5
Upper stretch: west tributary (3500-3180 m)	surface	13	0.8±0.3	46±31%	1.12±0.75	1.62±0.20	27±3%	65±3%	8±2%	2.0±0.3	1.2±0.5
	subsurface	3	0.4±0.0	47±14%	1.00±0.37	1.85±0.15	27±4%	59±5%	13±6%	2.7±0.8	2.3±0.8
Mid-stretch (3140-3040 m)	surface	8	1.1±0.7	43±30%	0.77±0.24	1.66±0.10	27±3%	58±3%	16±2%	3.0±0.3	1.9±0.5
	subsurface	4	1.2±0.5	85±14%	1.00±0.16	1.69±0.18	22±3%	64±3%	14±5%	2.9±0.8	1.7±0.9
	surface	3	1.3±0.8	44±31%	0.76±0.21	1.67±0.12	26±2%	60±5%	14±3%	2.8±0.4	2.4±0.1

Lower stretch
(3000-2940 m) subsurface 13 1.2±1.0 57±31% 0.81±0.40 1.84±0.21 22±4% 62±4% 15±3% 3.1±0.5 2.2±0.7

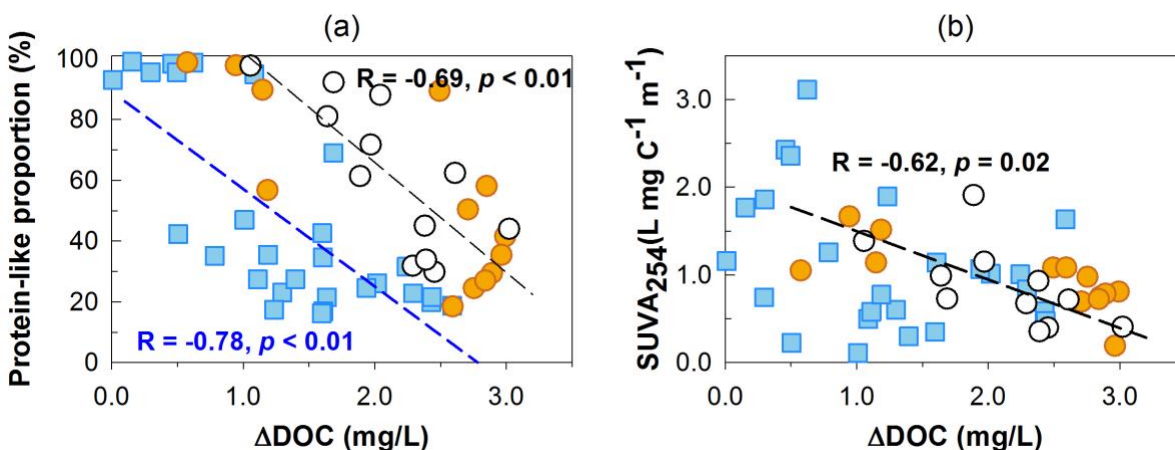
529 *Note. Surface represents stream and subsurface includes spring and groundwater. Data are reported as
530 averages ± standard deviation for each category.

531

532 3.4 Concurrent DOC Quantity and Quality Changes in Stream and Subsurface Waters

533 The loss of DOC (Δ DOC) in stream and subsurface waters, calculated by subtracting the
534 measured DOC concentration from an estimated initial DOC concentration based on mixing of
535 three-endmembers, represents DOC consumption along the flow paths in HLGW. In subsurface
536 waters where the effect of photodegradation is minimal, simultaneous decreases in the
537 proportions of protein-like fluorophores and SUVA₂₅₄ values are observed with increasing
538 Δ DOC (Fig. 3). For the stream waters, only the proportion of protein-like fluorophores is
539 correlated with Δ DOC, not SUVA₂₅₄ (Fig. 3). If only the upper stretches of the stream network
540 in HLGW are considered, the correlations between the proportions of protein-like fluorophores
541 and Δ DOC improve in the about 2-km long east ($r = -0.73$, $p = 0.002$) and west ($r = -0.78$, $p =$
542 0.003) tributaries, respectively. The lack of correlation between stream water SUVA₂₅₄ and
543 Δ DOC (Fig. 3) is likely due to stronger effect of photodegradation in surface water than in
544 groundwater due to aromatic C as light absorbing chromophores [Ward and Cory, 2016].

545 The concurrent changes in DOC quantity and quality are observed in the batch
546 experiments of four types of frozen soils collected from the HLGW. Consistent with the
547 concurrent changes in DOM quantity and quality in HLGW waters (Fig. 3), anoxic incubation of
548 four types of soil reveals utilization of protein-like components and aromatic carbon. Decrease
549 of SUVA₂₅₄ from > 4 to about $1 \text{ L mg C}^{-1} \text{ m}^{-1}$ and halving of protein-like fluorescent DOM is
550 found in 8 soil samples collected from the active layers of permafrost, the degraded permafrost
551 and thermokarst soils (Table S2). However, the soil incubations are compounded by
552 simultaneous release of DOM from SOC mobilization, and adsorption may also contribute to
553 DOC loss, making quantitative assessment impossible at this time, with details in Supporting
554 Information. When the first-order kinetic equation was applied to fit the SOC biodegradation
555 curves for the decrease in DOC in the second incubation experiment of the frost soil in the
556 reactor, the biodegradation constant of SOC (λ_{SOC}) is estimated to be 0.32 d^{-1} at $20 \text{ }^\circ\text{C}$, or a half-
557 time of 5 hours (Fig. S7).



559

560 **Figure 3.** (a) The proportion of protein-like component vs DOC loss (Δ DOC) in surface (blue)
 561 and subsurface (white and orange) water. (b) $SUVA_{254}$ vs DOC loss (Δ DOC) in surface (blue)
 562 and subsurface (white and orange) water. The blue and black dash lines represent the regression
 563 lines for stream and groundwater, respectively, with correlation coefficients marked next to the
 564 lines.

565

566 4 Discussion

567 4.1 Biodegradation Responsible for DOC Processing in Subsurface Environment

568 Δ DOC that represents DOC loss is estimated to evaluate to what extent DOM in HLGW
 569 is processed, based on the constraints of end-member analysis. Although glacier-snow and
 570 precipitation endmembers exhibit substantial uncertainties in their compositions (Table 2) due to
 571 altitudinal and temporal effects on isotopic compositions [Chang *et al.*, 2018; Li *et al.*, 2015],
 572 their effect on uncertainties of Δ DOC estimation is insignificant due to their low DOC content.
 573 In comparison, because the frozen soil endmember contains much more DOC than the glacier-
 574 snow and precipitation endmembers do, the uncertainty in Δ DOC estimation is mostly driven by
 575 the very small uncertainty of the soil endmember, and fortunately, is small (Table S1).

576 Both photodegradation and biodegradation can be important for mineralization of
 577 permafrost sourced DOC in high-altitude surface waters due to availability of sunlight [Wang
 578 *et al.*, 2018]. However, subsurface DOM is much less likely to undergo photo-oxidation or
 579 mineralization by sunlight, the DOC loss is therefore considered to mostly reflect biodegradation.
 580 The concurrent decreases of protein-like fluorophores and $SUVA_{254}$ with increasing DOC loss
 581 (Fig. 3) support the notion that aromatic DOM with high protein-like fluorophores, most likely

582 sourced from thawing of frozen soil, is subject to biodegradation in subsurface environment of
583 the HLGW. Further, the DOM quality changes in batch soil incubation support the utilization of
584 protein-like and aromatic C. While we cannot entirely rule out the possibility of photodegradation
585 due to frequent surface and subsurface water exchanges in HLGW, the transit time of subsurface
586 water should be longer than that of stream water, allowing for microbial processing time of DOM
587 in subsurface environment. The longer it takes for water to flow through subsurface, the higher
588 the DOC loss by microbial activities will be along this flow path. We take advantage of this
589 linkage to calculate MTT of groundwater using its Δ DOC obtained at the outlet of HLGW as
590 discussed in 4.2 next. The MTT reflects the flow pathways and water dynamics of the whole
591 system [McGuire *et al.*, 2005].

592

593 **4.2 Groundwater Mean Transit Time (MTT) in Response to Freeze-Thaw Cycles**

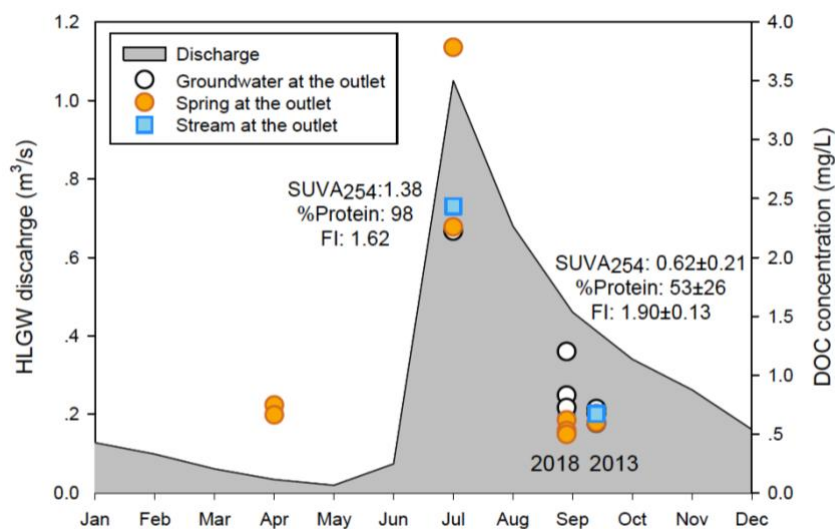
594 In the Arctic permafrost region, groundwater discharge is driven by soil freeze – thaw
595 processes with long water retention time [Ameli *et al.*, 2017; Ireson *et al.*, 2013; Walvoord and
596 Striegl, 2007] and horizontal flow path [Aiken *et al.*, 2014; O'Donnell *et al.*, 2012]. This longer
597 retention time explains the variable but usually low percentages of protein-like fluorophores:
598 0.3–22% in eight streams extending 250 km at Yenisei basin [Kawahigashi *et al.*, 2004]; 1–12%
599 over 500 km at Yukon basin and its small tributaries [O'Donnell *et al.*, 2010; Wickland *et al.*,
600 2012]. HLGW is small (25 km²) and alpine (11° topographical gradient) so the groundwater
601 MTT is expected to be short though not previously quantified. Only a handful of studies have
602 attempted to quantify mean transit time in hillslopes. MTT of days to weeks (10 – 25 days) has
603 been obtained for storm events, based on hydrometric and isotopic tracer approach in an alpine
604 watershed of Oregon [McGuire and McDonnell, 2010]. Very short transit time of 2 to 12 days is
605 observed for a mountain spring in Hong Kong constrained by radium (Ra) and radon (Rn)
606 isotopes along a steep slope [Luo and Jiao, 2019].

607 In the following, we first discuss qualitative evidence for MTT of groundwater in HLGW
608 responding to the seasonal freeze-thaw cycles followed by an attempt to quantify the MTT in
609 low and high discharge periods.

610 First, DOC concentrations of groundwater and spring collected at the same locations
611 close to the outlet of HLGW reach a maximum in July during peak discharge, higher than those

612 in September when discharge is much less (Fig. 4). The Δ DOC of these subsurface waters are
 613 $1.0 \pm 0.1 \text{ mg L}^{-1}$ in July and $2.5 \pm 0.4 \text{ mg L}^{-1}$ in September, respectively, suggesting lower loss in
 614 July than in September. This contrast is neither attributable to a difference in DOC_0 (July:
 615 $3.2 \pm 0.04 \text{ mg L}^{-1}$; September: $3.2 \pm 0.2 \text{ mg L}^{-1}$) nor to water temperature ($5 \text{ }^\circ\text{C}$). It is unlikely due
 616 to adsorption alone because DOM adsorption is rapid, and usually reaches equilibrium within a
 617 few minutes to hours [Gu et al., 1994; Kalbitz and Wennrich, 1998]. Further, retardation of DOM
 618 due to sorption only “delays” the arrival of influent DOC by 1.5 to 3 pore volumes in sandy to
 619 clayey columns [Li and Shuman, 1997]. Therefore, this retardation of DOC transport alone is
 620 unlikely to account for large changes in DOC concentrations at the outlet over 2 months (Fig. 4).

621



622

623 **Figure 4.** Monthly average stream discharge (left y-axis) in 2013 displayed in gray shade
 624 recorded at the gauging station (2960 m a.s.l) at the outlet of HLGW. Concentrations of DOC
 625 (right y-axis) in surface water (blue square) and springs (orange circles) and groundwater (white
 626 circles) from a monitoring well (MW – 30 m depth in Fig. 1d), all close to the gauging station,
 627 are higher in July than in September. Numbers are values of SUVA_{254} ($\text{L mg C}^{-1} \text{ m}^{-1}$), proportion
 628 of protein-like compound (%) and FI for groundwater from the MW.

629

630 Second, the protein-like proportion and SUVA_{254} of all subsurface waters at the outlet are
 631 higher in July ($98 \pm 0.5\%$, $1.25 \pm 0.41 \text{ L mg C}^{-1} \text{ m}^{-1}$, $n=3$) and lower in September ($45 \pm 23\%$,
 632 $0.66 \pm 0.26 \text{ L mg C}^{-1} \text{ m}^{-1}$, $n=10$). The inferred shorter MTT in July allows for more DOM with
 633 stronger permafrost DOM fingerprint to be detected in the subsurface environment. This change
 634 is especially clear when groundwaters repeatedly sampled from a single monitoring well
 635 screened at 30 m depth below ground (MW, see Fig.1d) in July 2013, September 2013 and 2018

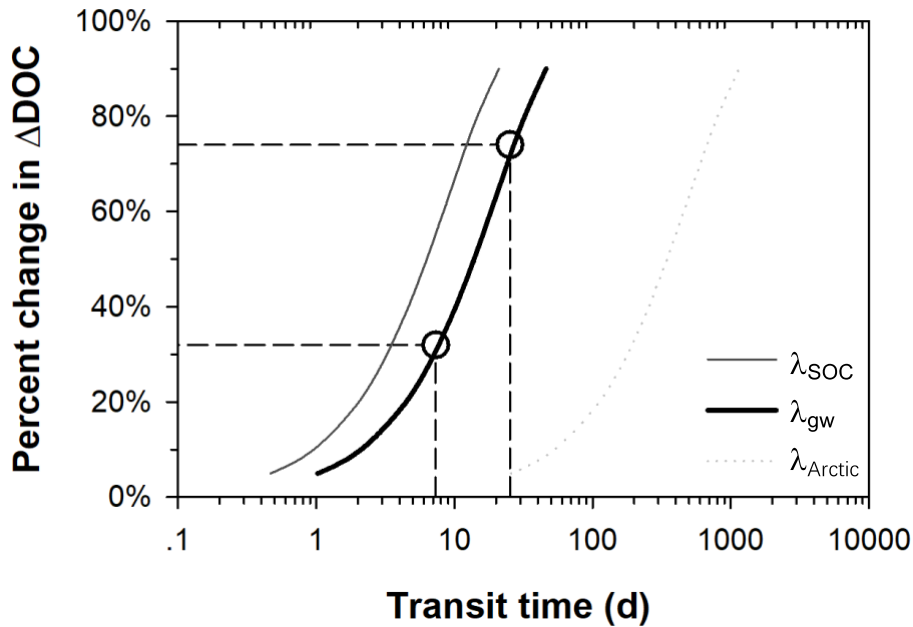
636 are considered (Fig. 4). Moreover, the DOC contrast in surface water is also consistent with this
637 difference in transit time (Fig. 4). The higher discharge and thus more extensive surface water
638 and groundwater interaction in July compared to September accelerates the already rapid
639 downward flow of groundwater in HLGW, also supported by field observation of the spring
640 discharge at the outlet of HLGW.

641 Third, an attempt is made to estimate groundwater MTT based on the DOC dynamics
642 described above, assuming subsurface biodegradation of DOC with first order kinetics (λ) that
643 is known to vary so the rationale for our choice is described. Incubation of 12 riverine DOM
644 samples yield λ from 0.147 to 0.781 d⁻¹ in headwater regions of the Yangtze, Yellow and
645 Lantsang -Mekong rivers [Ma *et al.*, 2018]. We adopt the average λ value of 0.25 d⁻¹ from 2
646 riverine DOM samples in 2 small alpine watersheds (94.3304°E, 35.75439° N) of the Yellow
647 River in Qinghai as the most likely for HLGW, given the similar topography, landscape (glacier
648 and permafrost), proximity (~ 500 km from HLGW), and comparable DOC concentration of
649 2.5±0.4 mg L⁻¹ and discharge of 1.27 m³/s [Ma *et al.*, 2018]. The λ becomes 0.06 d⁻¹ after
650 correcting to HLGW groundwater temperature of 5°C following the Arrhenius equation [Catalan
651 *et al.*, 2016]. Using 0.06 d⁻¹, the MTT is estimated to be approximately 6 days and 20 days in
652 July and September, respectively, corresponding to the changes in Δ DOC (Δ DOC/DOC₀)
653 observed for groundwater of monitoring well at HLGW outlet of 32% in July and 74% in
654 September (Fig. 5). Because most DOC entered the aquatic environment in the upper stretch of
655 HLGW (Fig. 1), this estimation of reaction time based on DOC degradation is thus indicative of
656 MTT for groundwater in HLGW.

657 Fourth, the sensitivity of MTT estimate to variable λ is described as follows. The SOC
658 degradation constant of 0.32 d⁻¹ established from our HLGW soil at 20°C is within the range of
659 λ from the 12 riverine DOM sample. However, incubation studies of Arctic water DOM have
660 found variable λ of 5×10⁻³ to 0.15 d⁻¹ [Balcarczyk *et al.*, 2009; Fellman *et al.*, 2008; Fellman *et al.*,
661 *et al.*, 2009; Spencer *et al.*, 2015]. The highest λ of 0.15 d⁻¹ is established from the first-order
662 streams of the Kolyma River, most likely to be representative of highly labile and freshly released
663 DOC in Arctic headwaters [Spencer *et al.*, 2015], and thus relevant. The slowest λ of 5×10⁻³ d⁻¹
664 is reported for incubation of DOM in the stream waters from large basins with long retention
665 time and Holocene deposit in Alaska at 4°C with in situ nutrients [Balcarczyk *et al.*, 2009].

666 Although these very long rates are unlikely, we have estimated the shortest and longest MTT
667 using the faster λ_{SOC} and slowest λ . The λ_{SOC} becomes 0.11 d^{-1} at 5°C after temperature correction,
668 and the MTT is estimated to be 3.5 d and 12.5 d for July and September, respectively (Fig. 5).
669 Based on the slowest λ of $5 \times 10^{-3} \text{ d}^{-1}$ the MTT can be as long as 200 d for July and 700 d for
670 September, respectively (Fig. 5).

671 There are several limitations to our MTT estimation. Given the degrees of spatial and
672 temporal variability in DOM quantity and quality, biodegradation kinetics of DOM warrants
673 further investigation. Perhaps more useful would be an independent assessment of groundwater
674 MTT using Ra-Rn isotopes [*Luo and Jiao, 2019*]. Further, changes in DOC and SUVA₂₅₄ from
675 our soil incubation experiments suggest release of aromatic carbon (Table S2). This raises the
676 yet to be assessed possibility that preferential sorption of highly aromatic carbon or humic-like
677 compounds onto soil or sediment may contribute to DOC loss along the groundwater flow path
678 [*Jin and Zimmerman, 2010*]. Finally, long-term observations of DOM quantity and quality are
679 desirable to reveal DOM dynamics that will allow separation of effects of gradual, seasonal
680 freeze-thaw cycles and abrupt, accelerated thawing of permafrost. These limitations are unlikely
681 to challenge the finding that subsurface DOM processing is primarily driven by biodegradation,
682 and the rate constants are similar in July and September. If so, the results are interpreted to
683 suggest that MTT in hillslopes vary in response to discharge corresponding to season freeze-
684 thaw cycles.



685

686 **Figure 5.** Percent changes in ΔDOC vs MTT (d) shown in log scale. Black line is for the most
 687 likely biodegradation rate constant (λ_{gw}) of 0.06 d^{-1} . The different groundwater MTT is shown
 688 as white circles to reflect percent changes in ΔDOC observed at MW in July (32%) and
 689 September (74%), respectively. The gray line to the left indicates a constant (λ_{SOC}) of 0.11 d^{-1}
 690 at 5°C based on HLGW soil incubation experiment. The dotted gray line (λ_{Arctic}) to the right
 691 indicates that MTT estimates using the lowest observed λ of $5 \times 10^{-3} \text{ d}^{-1}$ based on incubation of
 692 Arctic stream water samples [Balcarczyk *et al.*, 2009].

693

694 **4.3 Hillslopes Act as Hotspots of Permafrost Derived DOC Processing in Subsurface** 695 **Environment**

696 Although better constraints on DOC degradation kinetics and repeated monthly sampling
 697 from June to December of groundwater would likely result in improved estimates of mean transit
 698 time in HLGW, the results nevertheless demonstrate that DOM in permafrost regions of the QTP
 699 can be used to shed light on hillslope hydrological process in its headwaters. A long-held view
 700 is that aquifer is dominated by water with older ages (> 3 months) compared to riverine systems
 701 of much younger water (< 3 months) [Jasechko *et al.*, 2017]. Recent studies suggest a component
 702 of groundwater is very young in age [Gleeson *et al.*, 2016], yet unraveling the age distribution is
 703 currently challenging with long-term tracer observations [Luo and Jiao, 2019; McDonnell *et al.*,
 704 2010]. Though fraught with uncertainties, the estimation above is addressing a challenging

705 problem, and represents the first attempt to quantify hillslope groundwater transit time in the
706 QTP. A global evaluation has shown that the DOC decomposition rate in inland waters ranges
707 from 0.0003 to 9 d⁻¹ corresponding to a water retention time of 0.04 day to 42 years [*Catalan et*
708 *al.*, 2016]. This study supports the notion that hillslopes are hotspots for DOC processing with
709 subsurface environment playing an important role, expanding the coverage of the aforementioned
710 global evaluation to include an important inland water system in QTP.

711 Existing and newly gained insights on groundwater flow system in HLGW suggest
712 extensive surface water and groundwater interaction, supported by modeling [*Evans et al.*, 2015],
713 isotopic [*Ma et al.*, 2017], hydrochemical [*Li et al.*, 2014; *Li et al.*, 2016] and now DOM quantity
714 and quality data. These studies have identified shallow groundwater sourced primarily from
715 glacier-snow and precipitation [*Chang et al.*, 2018], and flows down gradient above permafrost
716 layer and later above the clay layer (Fig. 1d) [*Evans et al.*, 2015; *Ma et al.*, 2017].
717 Hydrogeological studies have shown that the subsurface water's radiocarbon age is modern and
718 contains tritium (³H) at shallow depth (<20 m) in permafrost and seasonal frost zones of the
719 HLGW [*Ma et al.*, 2017]. This understanding of groundwater flow together with its extensive
720 interaction with surface water is taken as representative of headwater watersheds with permafrost
721 of alpine hillslopes in the entire QTP. Considering the significantly lower DOC loss in July than
722 that in September based on differences in ΔDOC, the DOC fluxes were estimated for July and
723 other months, June to December except July. This assumes that September is representative of
724 other months which have lower discharges (Fig. 4), and the input and export of water is mass
725 balanced thus the same. Fluxes between January and May are not considered because the
726 discharge is very low and the soil is frozen.

727 We put this all together to estimate DOC input and output fluxes to illustrate the extent
728 of DOC loss in HLGW. In July, the DOC export is estimated to be 6.8×10³ kg by multiplying
729 monthly discharge and DOC concentration of 2.4 mg L⁻¹ from the outlet stream water of HLGW
730 (Table 4). We assume that the discharge of the HLGW outlet equals to the total of water recharge
731 from the three end-members to meet the volume balance. We take the DOC mass of glacier-snow
732 melting water as an example to present the estimation of DOC input. The input water volume is
733 calculated as total discharge of 2.8 ×10⁶ m³ multiplying its contribution fraction of 23% in the
734 outlet water sample. The input DOC mass of 0.3×10³ kg is based on the DOC value in glacier

735 end member of 0.5 mg L⁻¹ multiplying the water volume. Therefore, the DOC input flux is
 736 8.4×10³ kg, with the glacier-snow meltwater, precipitation, and soil meltwater contributing
 737 0.3×10³, 1.7×10³ and 6.4×10³ kg, respectively (Table 4). Between June to December excluding
 738 July, the DOC concentration of 0.7 mg L⁻¹ in September is representative for these months. The
 739 DOC export is 3.5×10³ kg, and the DOC input is 15.1×10³ kg with the glacier-snow meltwater,
 740 precipitation, and soil melt water contributing 0.6×10³ kg, 3.1×10³ kg and 11.4×10³ kg,
 741 respectively (Table 4). The annual DOC input flux is 23.5×10³ kg yr⁻¹, with an annual DOC
 742 export flux of 10.3 ×10³ kg yr⁻¹. The difference between input and export DOC fluxes is taken to
 743 represent a “lost” DOC flux of 13.2 ×10³ kg yr⁻¹ within HLGW before transporting into large
 744 rivers (Fig. 1c and Table 4). About half of the DOC is processed in hillslopes of small alpine
 745 watersheds, comprising a substantial fraction in C cycling in permafrost region under warming
 746 and warrant further attention.

747

748

Table 4. Input, export and respired DOC fluxes from HLGW.

Input DOC from three endmembers								
End members	DOC (mg/L)	Fraction	July		June-Dec w/o July *		Annual flux (10 ³ kg/yr)	
			Water vol. (10 ⁶ m ³)	DOC mass (10 ³ kg)	Water vol. (10 ⁶ m ³)	DOC mass (10 ³ kg)		
G	0.5	23%	0.65	0.3	1.16	0.6		
P	1.0	62%	1.74	1.7	3.12	3.1		
S	15.0	15%	0.42	6.4	0.76	11.4		
Input DOC (x10 ³ kg)			8.4		15.1		23.5	
Export DOC at the outlet of HLGW								
Stream at outlet	DOC (mg/L)	Water vol. (10 ⁶ m ³)	DOC mass (10 ³ kg)	June-Dec w/o July			Annual flux (10 ³ kg/yr)	
				DOC (mg/L)	Water vol. (10 ⁶ m ³)	DOC mass (10 ³ kg)		
Export DOC (x10 ³ kg)	2.4	2.8	6.8	0.7	5.0	3.5	10.3	
Loss of DOC during in-stream processing								
Loss of DOC (10 ³ kg)	July		June-Dec w/o July			Annual		
	1.6		11.6			13.2		
% lost DOC		19%		77%		56%		

749

750

751

* Input and output DOC between January and May are not considered due to seasonal freeze.

752 **Acknowledgments and Data**

753 We thank field team, Qixin Chang, Yalu Hu and Zhao Pan of CUG; Yu Xia, Chenyuan
754 Dang and Ziqi Wu of SUSTech, and staff at the Qilian Station of CAS for their help with the
755 fieldwork and for logistic assistance and quality time; Tom Streckas and Bob Engel of Queens
756 College, CUNY for access to UV-Vis; Junjian Wang of SUSTech for access to TOC-L; Penghui
757 Li and Zhen Tan for valuable discussion on PARAFAC. This study is supported by the National
758 Natural Science Foundation (NSFC Grants No. 41772265, 41831279 and 41228003). All data
759 are compiled and submitted in datasets S1 and S2 of supporting information, and will be archived
760 in SUSTech open research data repository under Science Data Bank
761 (<http://www.dx.doi.org/10.11922/sciencedb.o00005.00007>). We thank the editor and two
762 anonymous reviewers for their constructive comments.

763 **Reference**

- 764 Aiken, G. R., R. G. M. Spencer, R. G. Striegl, P. F. Schuster, and P. A. Raymond (2014), Influences of
765 glacier melt and permafrost thaw on the age of dissolved organic carbon in the Yukon River basin,
766 *Global Biogeochemical Cycles*, 28(5), 525-537.
- 767 Ameli, A. A., K. Beven, M. Erlandsson, I. F. Creed, J. J. McDonnell, and K. Bishop (2017), Primary
768 weathering rates, water transit times, and concentration-discharge relations: A theoretical analysis for the
769 critical zone, *Water Resources Research*, 53(1), 942-960.
- 770 Balcarczyk, K. L., J. B. Jones, R. Jaffé, and N. Maie (2009), Stream dissolved organic matter bioavailability
771 and composition in watersheds underlain with discontinuous permafrost, *Biogeochemistry*, 94(3), 255-
772 270.
- 773 Barnes, R. T., D. E. Butman, H. F. Wilson, and P. A. Raymond (2018), Riverine Export of Aged Carbon Driven
774 by Flow Path Depth and Residence Time, *Environmental Science & Technology*, 52(3), 1028-1035.
- 775 Benettin, P., J. W. Kirchner, A. Rinaldo, and G. Botter (2015), Modeling chloride transport using travel time
776 distributions at Plynlimon, Wales, *Water Resources Research*, 51(5), 3259-3276.
- 777 Brogi, S. R., S.-Y. Ha, K. Kim, M. Derrien, Y. K. Lee, and J. Hur (2018), Optical and molecular
778 characterization of dissolved organic matter (DOM) in the Arctic ice core and the underlying seawater
779 (Cambridge Bay, Canada): Implication for increased autochthonous DOM during ice melting, *Science of
780 the Total Environment*, 627, 802-811.
- 781 Catala, T. S., et al. (2015), Turnover time of fluorescent dissolved organic matter in the dark global ocean,
782 *Nature Communications*, 6.
- 783 Catalan, N., R. Marce, D. N. Kothawala, and L. J. Tranvik (2016), Organic carbon decomposition rates
784 controlled by water retention time across inland waters, *Nature Geoscience*, 9(7), 501-+.
- 785 Chang, Q., R. Ma, Z. Sun, A. Zhou, Y. Hu, and Y. Liu (2018), Using Isotopic and Geochemical Tracers to
786 Determine the Contribution of Glacier-Snow Meltwater to Streamflow in a Partly Glacierized Alpine-
787 Gorge Catchment in Northeastern Qinghai-Tibet Plateau, *Journal of Geophysical Research-Atmospheres*,
788 123(18), 10037-10056.
- 789 Cheng, G., and T. Wu (2007), Responses of permafrost to climate change and their environmental significance,
790 *Qinghai-Tibet Plateau, Journal of Geophysical Research*, 112(F2).
- 791 Coble, P. G. (1996), Characterization of marine and terrestrial DOM in seawater using excitation emission
792 matrix spectroscopy, *Marine Chemistry*, 51(4), 325-346.
- 793 Connolly, C. T., M. B. Cardenas, G. A. Burkart, R. G. M. Spencer, and J. W. McClelland (2020), Groundwater
794 as a major source of dissolved organic matter to Arctic coastal waters, *Nature Communications*, 11(1).
- 795 Cory, R. M., and D. M. McKnight (2005), Fluorescence Spectroscopy Reveals Ubiquitous Presence of
796 Oxidized and Reduced Quinones in Dissolved Organic Matter, *Environmental Science & Technology*,
797 39(21), 8142-8149.
- 798 Drake, T. W., P. A. Raymond, and R. G. M. Spencer (2018), Terrestrial carbon inputs to inland waters: A
799 current synthesis of estimates and uncertainty, *Limnology and Oceanography Letters*, 3(3), 132-142.
- 800 Drake, T. W., K. P. Wickland, R. G. M. Spencer, D. M. McKnight, and R. G. Striegl (2015), Ancient low-
801 molecular-weight organic acids in permafrost fuel rapid carbon dioxide production upon thaw,
802 *PROCEEDINGS OF THE NATIONAL ACADEMY OF SCIENCES*.
- 803 Evans, S. G., S. Ge, and S. Liang (2015), Analysis of groundwater flow in mountainous, headwater catchments
804 with permafrost, *Water Resources Research*, 51(12), 9564-9576.
- 805 Fellman, J. B., D. V. D'Amore, E. Hood, and R. D. Boone (2008), Fluorescence characteristics and
806 biodegradability of dissolved organic matter in forest and wetland soils from coastal temperate watersheds
807 in southeast Alaska, *Biogeochemistry*, 88(2), 169-184.
- 808 Fellman, J. B., E. Hood, R. T. Edwards, and D. V. D'Amore (2009), Changes in the concentration,
809 biodegradability, and fluorescent properties of dissolved organic matter during stormflows in coastal
810 temperate watersheds, *Journal of Geophysical Research-Biogeosciences*, 114.
- 811 Feng, L., J. Xu, S. Kang, X. Li, Y. Li, B. Jiang, and Q. Shi (2016), Chemical Composition of Microbe-Derived
812 Dissolved Organic Matter in Cryoconite in Tibetan Plateau Glaciers: Insights from Fourier Transform Ion
813 Cyclotron Resonance Mass Spectrometry Analysis, *Environmental Science & Technology*, 50(24),
814 13215-13223.

815 Frey, K. E., and J. W. McClelland (2009), Impacts of permafrost degradation on arctic river biogeochemistry,
816 Hydrological Processes, 23(1), 169-182.

817 Froehlich, K., M. Kralik, W. Papesch, D. Rank, H. Scheifinger, and W. Stichler (2008), Deuterium excess in
818 precipitation of Alpine regions - moisture recycling, *Isotopes in Environmental and Health Studies*, 44(1),
819 61-70.

820 Ge, S., J. McKenzie, C. Voss, and Q. Wu (2011), Exchange of groundwater and surface-water mediated by
821 permafrost response to seasonal and long term air temperature variation, *Geophysical Research Letters*,
822 38.

823 Genereux, D. (1998), Quantifying uncertainty in tracer-based hydrograph separations, *Water Resources*
824 *Research*, 34(4), 915-919.

825 Gleeson, T., K. M. Befus, S. Jasechko, E. Luijendijk, and M. B. Cardenas (2016), The global volume and
826 distribution of modern groundwater, *Nature Geoscience*, 9(2), 161-+.

827 Gonçalvesaraujo, R., M. A. Granskog, A. Bracher, K. Azetsuscott, P. A. Dodd, and C. A. Stedmon (2016),
828 Using fluorescent dissolved organic matter to trace and distinguish the origin of Arctic surface waters,
829 *Scientific Reports*, 6(33978), 33978.

830 Green, S. A., and N. V. Blough (1994), Optical absorption and fluorescence properties of chromophoric
831 dissolved organic matter in natural waters, *Limnology and Oceanography*, 39(8), 1903-1916.

832 Gu, B. H., J. Schmitt, Z. H. Chen, L. Y. Liang, and J. F. McCarthy (1994), ADSORPTION AND
833 DESORPTION OF NATURAL ORGANIC-MATTER ON IRON-OXIDE - MECHANISMS AND
834 MODELS, *Environmental Science & Technology*, 28(1), 38-46.

835 Guo, L., and R. W. Macdonald (2006), Source and transport of terrigenous organic matter in the upper Yukon
836 River: Evidence from isotope ($\delta^{13}C$, $\Delta^{14}C$, and $\delta^{15}N$) composition of dissolved, colloidal, and
837 particulate phases, *Global Biogeochemical Cycles*, 20(2).

838 Guo, L., C.-L. Ping, and R. W. Macdonald (2007), Mobilization pathways of organic carbon from permafrost
839 to arctic rivers in a changing climate, *Geophysical Research Letters*, 34(13), n/a-n/a.

840 Heslop, J. K., M. Winkel, K. M. Walter Anthony, R. G. M. Spencer, D. C. Podgorski, P. Zito, A. Kholodov,
841 M. Zhang, and S. Liebner (2019), Increasing Organic Carbon Biolability With Depth in Yedoma
842 Permafrost: Ramifications for Future Climate Change, *Journal of Geophysical Research: Biogeosciences*,
843 124(7), 2021-2038.

844 Hu, Y., R. Ma, Y. Wang, Q. Chang, S. Wang, M. Ge, J. Bu, and Z. Sun (2019), Using hydrogeochemical data
845 to trace groundwater flow paths in a cold alpine catchment, *Hydrological Processes*.

846 Ireson, A. M., G. van der Kamp, G. Ferguson, U. Nachshon, and H. S. Wheater (2013), Hydrogeological
847 processes in seasonally frozen northern latitudes: understanding, gaps and challenges, *Hydrogeology*
848 *Journal*, 21(1), 53-66.

849 Jasechko, S., et al. (2017), Global aquifers dominated by fossil groundwaters but wells vulnerable to modern
850 contamination, *Nature Geoscience*, 10(6), 425-+.

851 Jin, J., and A. R. Zimmerman (2010), Abiotic interactions of natural dissolved organic matter and carbonate
852 aquifer rock, *Applied Geochemistry*, 25(3), 472-484.

853 Kalbitz, K., and R. Wennrich (1998), Mobilization of heavy metals and arsenic in polluted wetland soils and
854 its dependence on dissolved organic matter, *Science of the Total Environment*, 209(1), 27-39.

855 Kawahigashi, M., K. Kaiser, K. Kalbitz, A. Rodionov, and G. Guggenberger (2004), Dissolved organic matter
856 in small streams along a gradient from discontinuous to continuous permafrost, *Global Change Biology*,
857 10(9), 1576-1586.

858 Li, C., F. Yan, S. Kang, P. Chen, Z. Hu, X. Han, G. Zhang, S. Gao, B. Qu, and M. Sillanpaa (2017), Deposition
859 and light absorption characteristics of precipitation dissolved organic carbon (DOC) at three remote
860 stations in the Himalayas and Tibetan Plateau, China, *Science of the Total Environment*, 605, 1039-1046.

861 Li, C., et al. (2018), Fossil Fuel Combustion Emission From South Asia Influences Precipitation Dissolved
862 Organic Carbon Reaching the Remote Tibetan Plateau: Isotopic and Molecular Evidence, *Journal of*
863 *Geophysical Research-Atmospheres*, 123(11), 6248-6258.

864 Li, Z., F. Qi, Q. J. Wang, Y. Song, L. Hongyi, and L. Yongge (2016), The influence from the shrinking
865 cryosphere and strengthening evapotranspiration on hydrologic process in a cold basin, Qilian Mountains,
866 *Global and Planetary Change*, 144, 119-128.

867 Li, Z., F. Qi, L. Wei, W. Tingting, C. Aifang, G. Yan, G. Xiaoyan, P. Yanhui, L. Jianguo, and G. Rui (2014),
868 Study on the contribution of cryosphere to runoff in the cold alpine basin: A case study of Hulugou River
869 Basin in the Qilian Mountains, *Global and Planetary Change*, 122, 345-361.

870 Li, Z., et al. (2015), The stable isotope evolution in Shiyi glacier system during the ablation period in the north
871 of Tibetan Plateau, China, *Quaternary International*, 380, 262-271.

872 Li, Z. B., and L. M. Shuman (1997), Estimation of retardation factor of dissolved organic carbon in sandy soils
873 using batch experiments, *Geoderma*, 78(3-4), 197-206.

874 Luo, X., and J. J. Jiao (2019), Unraveling controlling factors of concentration discharge relationships in a
875 fractured aquifer dominant spring-shed: Evidence from mean transit time and radium reactive transport
876 model, *Journal of Hydrology*, 571, 528-544.

877 Ma, R., Z. Sun, Y. Hu, Q. Chang, S. Wang, W. Xing, and M. Ge (2017), Hydrological connectivity from
878 glaciers to rivers in the Qinghai-Tibet Plateau: roles of suprapermafrost and subpermafrost groundwater,
879 *Hydrology and Earth System Sciences*, 21(9), 4803-4823.

880 Ma, X., G. Liu, X. Wu, H. Xu, L. Ye, X. Zhang, W. ai (2018), Bioavailability of Dissolved Organic Carbon
881 in Rivers for Typical Vegetation Types in the Permafrost Regions on the Qinghai-Tibet Plateau,
882 *Environmental Science*, 39(5), 2086-2094. Doi 10.13227/j.hjx.201709280. (in Chinese)

883 Mann, P. J., T. I. Eglinton, C. P. McIntyre, N. Zimov, A. Davydova, J. E. Vonk, R. M. Holmes, and R. G. M.
884 Spencer (2015), Utilization of ancient permafrost carbon in headwaters of Arctic fluvial networks, *Nature*
885 *Communications*, 6.

886 McDonnell, J. J., et al. (2010), How old is streamwater? Open questions in catchment transit time
887 conceptualization, modelling and analysis, *Hydrological Processes*, 24(12), 1745-1754.

888 McGuire, A. D., L. G. Anderson, T. R. Christensen, S. Dallimore, L. Guo, D. J. Hayes, M. Heimann, T. D.
889 Lorenson, R. W. Macdonald, and N. Roulet (2009), Sensitivity of the carbon cycle in the Arctic to climate
890 change, *Ecological Monographs*, 79(4), 523-555.

891 McGuire, A. D., et al. (2018), Dependence of the evolution of carbon dynamics in the northern permafrost
892 region on the trajectory of climate change, *Proceedings of the National Academy of Sciences of the United*
893 *States of America*, 115(15), 3882-3887.

894 McGuire, K. J., and J. J. McDonnell (2010), Hydrological connectivity of hillslopes and streams: Characteristic
895 time scales and nonlinearities, *Water Resources Research*, 46.

896 McGuire, K. J., J. J. McDonnell, M. Weiler, C. Kendall, B. L. McGlynn, J. M. Welker, and J. Seibert (2005),
897 The role of topography on catchment-scale water residence time, *Water Resources Research*, 41(5).

898 McKnight, D. M., E. W. Boyer, P. K. Westerhoff, P. T. Doran, T. Kulbe, and D. T. Andersen (2001),
899 Spectrofluorometric characterization of dissolved organic matter for indication of precursor organic
900 material and aromaticity, *Limnology and Oceanography*, 46(1), 38-48.

901 Murphy, K. R., C. A. Stedmon, D. T. Waite, and G. M. Ruiz (2008), Distinguishing between terrestrial and
902 autochthonous organic matter sources in marine environments using fluorescence spectroscopy, *Marine*
903 *Chemistry*, 108(1-2), 40-58.

904 Murphy, K. R., C. A. Stedmon, D. Graeber, and R. Bro (2013), Fluorescence spectroscopy and multi-way
905 techniques. PARAFAC, *Anal. Methods*, 5(23), 6557-6566.

906 Murphy, K. R., C. A. Stedmon, P. Wenig, and R. Bro (2014), OpenFluor- an online spectral library of auto-
907 fluorescence by organic compounds in the environment, *Anal. Methods*, 6(3), 658-661.

908 Neff, J. C., J. C. Finlay, S. A. Zimov, S. P. Davydov, J. J. Carrasco, E. A. G. Schuur, and A. I. Davydova
909 (2006), Seasonal changes in the age and structure of dissolved organic carbon in Siberian rivers and
910 streams, *Geophysical Research Letters*, 33(23).

911 O'Donnell, J. A., G. R. Aiken, E. S. Kane, and J. B. Jones (2010), Source water controls on the character and
912 origin of dissolved organic matter in streams of the Yukon River basin, Alaska, *Journal of Geophysical*
913 *Research*, 115(G3).

914 O'Donnell, J. A., G. R. Aiken, M. A. Walvoord, and K. D. Butler (2012), Dissolved organic matter composition
915 of winter flow in the Yukon River basin: Implications of permafrost thaw and increased groundwater
916 discharge, *Global Biogeochemical Cycles*, 26.

917 Parlanti, E., K. Wörz, L. Geoffroy, and M. Lamotte (2000), Dissolved organic matter fluorescence
918 spectroscopy as a tool to estimate biological activity in a coastal zone submitted to anthropogenic inputs,
919 *Organic Geochemistry*, 31(12), 1765-1781.

920 Plaza, C., et al. (2019), Direct observation of permafrost degradation and rapid soil carbon loss in tundra,
921 Nature Geoscience, 12(8), 627-631.

922 Raymond, P. A., and R. G. M. Spencer (2015), Riverine DOM, 509,525-533 pp.

923 Raymond, P. A., et al. (2013), Global carbon dioxide emissions from inland waters, Nature, 503(7476), 355-
924 359.

925 Spencer, R. G. M., W. Guo, P. A. Raymond, T. Dittmar, E. Hood, J. Fellman, and A. Stubbins (2014), Source
926 and biolability of ancient dissolved organic matter in glacier and lake ecosystems on the Tibetan Plateau,
927 Geochimica et Cosmochimica Acta, 142, 64-74.

928 Spencer, R. G. M., P. J. Mann, T. Dittmar, T. I. Eglington, C. McIntyre, R. M. Holmes, N. Zimov, and A.
929 Stubbins (2015), Detecting the signature of permafrost thaw in Arctic rivers, Geophysical Research
930 Letters, 42(8), 2830-2835.

931 Stedmon, C. A., and R. Bro (2008), Characterizing dissolved organic matter fluorescence with parallel factor
932 analysis: a tutorial, Limnology and Oceanography-methods, 6(11), 572-579.

933 Stedmon, C. A., D. N. Thomas, S. Papadimitriou, M. A. Granskog, and G. S. Dieckmann (2011), Using
934 fluorescence to characterize dissolved organic matter in Antarctic sea ice brines, Journal of Geophysical
935 Research-Biogeosciences, 116.

936 Striegl, R. G., G. R. Aiken, M. M. Dornblaser, P. A. Raymond, and K. P. Wickland (2005), A decrease in
937 discharge-normalized DOC export by the Yukon River during summer through autumn, Geophysical
938 Research Letters, 32(21).

939 Tarnocai, C., J. G. Canadell, E. A. G. Schuur, P. Kuhry, G. Mazhitova, and S. Zimov (2009), Soil organic
940 carbon pools in the northern circumpolar permafrost region, Global Biogeochemical Cycles, 23.

941 Turetsky, M. R., et al. (2020), Carbon release through abrupt permafrost thaw, Nature Geoscience, 13(2), 138-
942 143.

943 Vonk, J., S. Tank, and M. Walvoord (2019), Integrating hydrology and biogeochemistry across frozen
944 landscapes, Nature Communications, 10.

945 Vonk, J. E., et al. (2013), High biolability of ancient permafrost carbon upon thaw, Geophysical Research
946 Letters, 40(11), 2689-2693.

947 Walvoord, M. A., and R. G. Striegl (2007), Increased groundwater to stream discharge from permafrost
948 thawing in the Yukon River basin: Potential impacts on lateral export of carbon and nitrogen, Geophysical
949 Research Letters, 34(12).

950 Wang, T., D. Yang, Y. Yang, S. Piao, X. Li, G. Cheng, and B. Fu (2020), Permafrost thawing puts the frozen
951 carbon at risk over the Tibetan Plateau, Science Advances, 6(19).

952 Wang, Y., R. G. M. Spencer, D. C. Podgorski, A. M. Kellerman, H. Rashid, P. Zito, W. Xiao, D. Wei, Y.
953 Yang, and Y. Xu (2018), Spatiotemporal transformation of dissolved organic matter along an alpine
954 stream flow path on the Qinghai-Tibet Plateau: importance of source and permafrost degradation,
955 Biogeosciences, 15(21), 6637-6648.

956 Ward, C. P., and R. M. Cory (2016), Complete and Partial Photo-oxidation of Dissolved Organic Matter
957 Draining Permafrost Soils, Environmental Science & Technology, 50(7), 3545-3553.

958 Weishaar, J. L., G. R. Aiken, B. A. Bergamaschi, M. S. Fram, R. Fujii, and K. Mopper (2003), Evaluation of
959 specific ultraviolet absorbance as an indicator of the chemical composition and reactivity of dissolved
960 organic carbon, Environmental Science & Technology, 37(20), 4702-4708.

961 Wickland, K. P., G. R. Aiken, K. Butler, M. M. Dornblaser, R. G. M. Spencer, and R. G. Striegl (2012),
962 Biodegradability of dissolved organic carbon in the Yukon River and its tributaries: Seasonality and
963 importance of inorganic nitrogen, Global Biogeochemical Cycles, 26(4).

964 Wunsch, U. J., J. K. Geuer, O. J. Lechtenfeld, B. P. Koch, K. R. Murphy, and C. A. Stedmon (2018),
965 Quantifying the impact of solid-phase extraction on chromophoric dissolved organic matter composition,
966 Marine Chemistry, 207, 33-41.

967 Xu, J., Q. Zhang, X. Li, X. Ge, C. Xiao, J. Ren, and D. Qin (2013), Dissolved Organic Matter and Inorganic
968 Ions in a Central Himalayan Glacier-Insights into Chemical Composition and Atmospheric Sources,
969 Environmental Science & Technology, 47(12), 6181-6188.

970 Yang, M., F. E. Nelson, N. I. Shiklomanov, D. Guo, and G. Wan (2010), Permafrost degradation and its
971 environmental effects on the Tibetan Plateau: A review of recent research, Earth-Science Reviews, 103(1-
972 2), 31-44.

- 973 Yao, Y., C. Zheng, C. Andrews, Y. Zheng, A. Zhang, and J. Liu (2017), What controls the partitioning between
974 baseflow and mountain block recharge in the Qinghai-Tibet Plateau?, *Geophysical Research Letters*,
975 44(16), 8352-8358.
- 976 Yi, S., Q. Wang, and W. Sun (2016), Basin mass dynamic changes in China from GRACE based on a
977 multibasin inversion method, *Journal of Geophysical Research-Solid Earth*, 121(5), 3782-3803.
- 978 Zhang, G., et al. (2017), Lake volume and groundwater storage variations in Tibetan Plateau's endorheic basin,
979 *Geophysical Research Letters*, 44(11), 5550-5560.
- 980 Zhang, X., J. A. Hutchings, T. S. Bianchi, Y. Liu, A. R. Arellano, and E. A. G. Schuur (2017), Importance of
981 lateral flux and its percolation depth on organic carbon export in Arctic tundra soil: Implications from a
982 soil leaching experiment, 122(4), 796-810.